

AD-754 073

AN ANALYTICAL AND EXPERIMENTAL INVESTI-
GATION OF ROTATING, NON-CAPILLARY HEAT
PIPES

Paul J. Marto

Naval Postgraduate School

Prepared for:

National Aeronautics and Space Administration

30 November 1972

DISTRIBUTED BY:

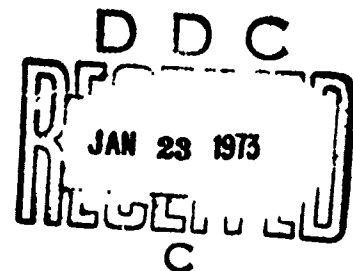
NTIS

National Technical Information Service
U. S. DEPARTMENT OF COMMERCE
5285 Port Royal Road, Springfield Va. 22151

NAVAL POSTGRADUATE SCHOOL

Monterey, California

AD754073



Reproduced by
NATIONAL TECHNICAL
INFORMATION SERVICE
U S Department of Commerce
Springfield VA 22151

AN ANALYTICAL AND EXPERIMENTAL
INVESTIGATION OF ROTATING, NON-CAPILLARY
HEAT PIPES

FINAL REPORT

by

P. J. MARTO
30 NOVEMBER 1972

Approved for public release; distribution unlimited.

64
7

ACKNOWLEDGEMENT

The author would like to thank his thesis students L. J. Ballback, T. J. Daley, W. H. Newton, J. S. Woodard, and C. E. Schafer, whose sustained efforts contributed significantly to the results of this project. Thanks should also be given to the many technicians who helped fabricate and instrument the experimental equipment, in particular to Mr. R. Sheile, Mr. M. O'Day, and Mr. D. Harvey. Finally, the author would like to express his appreciation to Mr. Vernon H. Gray of the NASA, Lewis Research Center for his interest and encouragement throughout this work.

UNCLASSIFIED

Security Classification

DOCUMENT CONTROL DATA - R & D

(Security classification of title, body of abstract and indexing annotation must be entered when the overall report is classified)

1. ORIGINATING ACTIVITY (Corporate author) Naval Postgraduate School Monterey, California 93940		2a. REPORT SECURITY CLASSIFICATION Unclassified	
		2b. GROUP	
3. REPORT TITLE An Analytical and Experimental Investigation of Rotating, Non-Capillary Heat Pipes			
4. DESCRIPTIVE NOTES (Type of report and, inclusive dates) Final Report, September, 1969 - June, 1972			
5. AUTHOR(S) (First name, middle initial, last name) Paul J. Marto			
6. REPORT DATE 30 November 1972	7a. TOTAL NO. OF PAGES 67	7b. NO. OF REFS 21	
8a. CONTRACT OR GRANT NO.	8b. ORIGINATOR'S REPORT NUMBER(S) NPS - 59MX72111A		
8c. PROJECT NO. NASA, Defense Purchase Request W-13007	8d. OTHER REPORT NO(S) (Any other numbers that may be assigned this report)		
10. DISTRIBUTION STATEMENT This document has been approved for public release and sale; its distribution is unlimited.			
11. SUPPLEMENTARY NOTES		12. SPONSORING MILITARY ACTIVITY	
13. ABSTRACT An approximate theoretical model is derived for laminar film condensation on the inside of a rotating, truncated cone, and is used to predict the heat transfer performance of rotating, non-capillary heat pipes for a wide variety of parametric conditions. Experimental results are presented for water, ethyl alcohol and freon-113 in a stainless steel heat pipe rotating to speeds of 2800 RPM. Results show that these devices can be used effectively to transfer large quantities of heat in rotating systems. Predicted results agree to within ± 20 percent of the experimental data. Dropwise condensation, instead of film condensation, improves heat pipe performance, while the presence of non-condensable gases impairs performance.			

- 1 -

UNCLASSIFIED

Security Classification

4-81400

UNCLASSIFIED

Security Classification

14 KEY WORDS	LINK A		LINK B		LINK C	
	ROLE	WT	ROLE	WT	ROLE	WT
Heat Pipe, rotating						
Heat Pipe, wickless						
Film Condensation						
Condensation						
Thermosyphon						

- ii -

UNCLASSIFIED

Security Classification

A-31409

TABLE OF CONTENTS

	<u>Page</u>
1. INTRODUCTION	1
1.1 Objective	1
2. ANALYTICAL PROGRAM	2
2.1 Film Condensation Model	2
2.2 Analysis of Newton [10]	5
2.3 Heat Pipe Parametric Study	12
2.4 Summary of Analytical Results	14
3. EXPERIMENTAL PROGRAM	15
3.1 Description of Equipment	15
3.2 Experimental Procedures	21
3.3 Reduction of Data	23
4. EXPERIMENTAL RESULTS	24
4.1 Evaporator Performance	24
4.2 Condenser Performance	25
4.3 Comparison of Theory & Experiment	28
5. CONCLUSIONS & RECOMMENDATIONS	30
5.1 Conclusions	30
5.2 Recommendations	30
BIBLIOGRAPHY	32
INITIAL DISTRIBUTION LIST	57
FORM DD 1473	62

1. INTRODUCTION

One method of improving upon the performance of rotating machinery components such as motors, generators, turbines, and high speed bearings and drills is to provide internal cooling using the rotating, non-capillary heat pipe concept [1]¹.

The rotating, non-capillary heat pipe² is shown schematically in Figure 1. It consists of a sealed hollow shaft, having a slight internal taper from one end to the other, and containing a fixed amount of working fluid. When the shaft is rotated at high speed about its longitudinal axis, the working fluid collects as an annulus at the large end. The diameter may be stepped at this end to provide a larger liquid reservoir. Heat added to this end of the shaft (evaporator) evaporates the working fluid, generating vapor which then flows axially toward the other end. Heat removed from this end of the shaft (condenser) condenses the vapor. The centrifugal forces accelerate the liquid condensate back to the evaporator to complete the cycle.

1.1 OBJECTIVE

The overall objective of this research program is to understand the operating characteristics and to predict the heat transfer performance capabilities of the rotating, non-capillary heat pipe. Preliminary work under this program has been reported earlier [2]. This report presents the final results obtained, with some recommendations toward further work.

¹ Numbers in brackets indicate references listed in the Bibliography.

² This device should perhaps be called a rotating, two-phase, closed thermosyphon.

2. ANALYTICAL PROGRAM

The analytical program initially focused upon the understanding of the operation of the rotating, non-capillary heat pipe, including a study of the mechanisms of nucleate boiling and condensation heat transfer, and two-phase, annular, counter-current flow. The heat transfer limitations imposed upon the rotating, non-capillary heat pipe by (a) the critical nucleate boiling heat flux ("burnout"), (b) the vapor-condensate entrainment velocity ("flooding"), (c) the sonic vapor velocity, and (d) the film condensation thermal resistance were estimated and compared. It was concluded that the performance of these devices would be controlled primarily by the overall resistance to heat transfer in the condenser, including the internal film condensation resistance, the conduction resistance across the condenser wall, and the outside surface heat transfer resistance [2, 3, 4]. The rotating non-capillary heat pipe was then modelled as a rotating, truncated cone, and a Nusselt-type film condensation analysis was performed. (Figure 2)

2.1 FILM CONDENSATION MODEL

Laminar film condensation with rotation has been analyzed for a variety of geometrical conditions. In 1959, Sparrow and Gregg [5] obtained a similarity solution for film condensation on a rotating disk situated in a quiescent vapor. They formulated the problem as an exact solution of the Navier-Stokes and energy equations, and arrived at numerical results for a wide variety of test fluids. Later, in 1961, Sparrow and Hartnett [6] showed that the disk solution could be modified to apply to film

condensation on the outside of rotating cones which are not too slender. In 1963, Singer and Preckshot [7] studied condensation on the outside of a rotating shaft. They reported the presence of three condensate flow regimes, which depended on shaft speed, and theoretically estimated the heat transfer during two of the regimes. Chato [8], in 1965, studied film condensation in a variable gravity field during rotation of a condensing thermosyphon. He included the effect of surface shear between the liquid condensate and the moving vapor.

During this work, Ballback [3] performed a Nusselt-type analysis for film condensation on the inside of a rotating, truncated cone of half angle ϕ as modelled in Figure 2. Ballback made all the familiar assumptions used in Nusselt's theory of laminar film condensation, including negligible subcooling and momentum changes in the condensate film, no interfacial shear between the condensate and vapor, and pure conduction within the condensate film. In addition, he assumed that the centrifugal acceleration is much larger than the normal acceleration of earth gravity, the thickness of the film is much less than the radius of the condenser wall, and the vapor space is essentially stagnant. In order to analytically solve for the condensate film thickness, however, Ballback further assumed that the slope of the condensate film, $d\delta/dx$, is much less than $\tan \phi$. This last assumption is not valid for very small half-cone angles ϕ . He analytically solved for the condensate film thickness and heat transfer coefficient, and his results were later confirmed as a special case of the work of Dhir and Lienhard [9] who studied laminar film condensation on axisymmetric bodies in non-uniform gravity fields.

Daley [4] reasoned that most practical applications of the rotating, non-capillary heat pipe would involve very small half-cone angles. He

therefore modified Ballback's work by removing the restriction that $d\delta/dx$ is much less than $\tan \phi$. He also improved upon the analysis by including the thermal resistances due to the condenser wall and to the outside surface cooling mechanism. Using the velocity profile for the condensate developed by Ballback, Daley arrived at a non-linear second order differential equation for the film thickness, δ [2]. He numerically integrated this expression using a Runge-Kutta-Gill numerical integration scheme. To start the integration, he used the conditions that $\delta = \delta_i$ and $\frac{d\delta}{dx} = \tan \phi$ at $x = 0$. It was postulated that δ_i was a function of the over-fall condition at the step located at the condenser exit. Daley arrived at an expression for the minimum film thickness, δ_{min} at the condenser exit, using the approximation that the flow over the step approximated the free fall condition for open channel flow. Having found the film thickness from the second order differential equation at $x = L$, the condenser exit, Daley compared this value with δ_{min} at L . Using this technique, Daley was able to find the heat flow out of the condenser as a function of RPM for 0° half cone angle only. As the cone angle was increased to 1° , however, the numerical integration of the highly non-linear second order differential equation became extremely sensitive to the initial value of the film thickness. Consequently, no solutions were found for half cone angles greater than zero.

The Nusselt type film condensation analysis performed by Ballback and Daley was extended by Newton [10] to include the effects of vapor pressure drop and interfacial shear. Equations for momentum, continuity and energy were developed for an infinitesimal fluid element in the condensate, and, assuming one dimensional turbulent flow, momentum and

continuity equations were developed for isothermal vapor flow. The details of his analysis are now included for completeness.

2.2 ANALYSIS OF NEWTON[10]

Condensate Momentum Equations

Assuming that the momentum changes within the condensate film are small, a static force balance on a differential liquid element in the x-direction (See Figure 3) yields:

$$0 = \frac{\partial \tau}{\partial y} - \frac{\partial p}{\partial x} + \rho_f \omega^2 r \sin \phi \quad (1)$$

where

τ = local shear stress

p = local pressure

x = co-ordinate measuring distance along the condensing surface

y = co-ordinate measuring distance normal to the condensing surface

r = local radius in the condensate

ϕ = half-cone angle

ρ_f = density of the condensate film

ω = angular velocity

Similarly, a force balance in the y-direction yields:

$$0 = - \frac{\partial p}{\partial y} - \rho_f \omega^2 r \cos \phi \quad (2)$$

In the above equations, the local radius at any point in the liquid condensate may be expressed as:

$$r(x,y) = R_0 + x \sin \phi - y \cos \phi \quad (3)$$

where R_0 = minimum wall radius in the condenser section.

Newton [10] substituted Equation (3) for $r(x,y)$ into (2) and integrated from p to p_v and y to δ (the local condensate thickness) to obtain the local pressure at any point within the condensate:

$$p(x,y) = p_v(x) + \rho_f \omega^2 \cos \phi \{ (R_o + x \sin \phi) (\delta - y) - \frac{1}{2} \cos \phi (\delta^2 - y^2) \} \quad (4)$$

Differentiating Equation (4) with respect to x , substituting this result into Equation (1), and integrating from y to δ and τ to $-\tau_v$ gives:

$$\begin{aligned} \tau &= - \frac{dp_v}{dx} (\delta - y) - \tau_v + \rho_f \omega^2 [R_o + x \sin \phi - \delta \cos \phi] [\sin \phi - \cos \phi \frac{d\delta}{dx}] (\delta - y) \\ &= \mu_f \frac{\partial u(x,y)}{\partial y} \end{aligned} \quad (5)$$

where

μ_f = viscosity of the condensate film

$u(x,y)$ = velocity of the condensate film

Another integration from 0 to y and from 0 to u gives an expression for the velocity:

$$\begin{aligned} u(x,y) &= - \frac{1}{\mu_f} \frac{dp_v}{dx} (y\delta - \frac{y^2}{2}) - \frac{\tau_v}{\mu_f} y \\ &\quad + \frac{\rho_f \omega^2}{\mu_f} [R_o + x \sin \phi - \delta \cos \phi] [\sin \phi - \cos \phi \frac{d\delta}{dx}] (y\delta - \frac{y^2}{2}) \end{aligned} \quad (6)$$

Continuity Equation

Conservation of mass, with condensation occurring, requires that

$$\frac{dw_f}{dx} = \frac{dw_v}{dx} \quad (7)$$

or

$$w_f = w_v \quad (7a)$$

where

$$w_f = \text{mass rate of flow of condensate} \\ = \int_0^\delta \rho_f u(x,y) 2\pi r(x,y) dy \quad (8)$$

$$w_v = \text{mass rate of flow of vapor} \\ = \rho_v \pi R^2(x) v(x) \quad (9)$$

and

$$R(x) = R_0 + x \sin\phi - \delta \cos\phi \quad (10)$$

Energy Equation

An energy balance on the differential element may be written

as:

$$\frac{dq}{dx} = h_{fg} \frac{dw_f}{dx} = \frac{2\pi(R_0 + x \sin\phi) (T_s - T_\infty)}{\frac{\delta}{k_f} + \frac{t}{k_w} + \frac{1}{h}} \quad (11)$$

where

T_s = saturation temperature of the vapor

T_∞ = ambient coolant temperature

t = thickness of the condenser wall

δ = film thickness of the condensate

k_f = thermal conductivity of condensate film

k_w = thermal conductivity of condenser wall

h = external heat transfer coefficient

h_{fg} = latent heat of vaporization

q = heat transfer rate

Note that the above differential equation is only valid for small half-cone angles (where the condenser geometry is not too different from cylindrical) and for thin condenser walls.

Vapor Momentum Equation

Using the differential element shown in Figure 4, and neglecting the momentum contribution due to the condensing vapor, a balance of forces may be taken in the x-direction and set equal to vapor momentum changes:

$$-A_v \frac{dp_v}{dx} + \tau_v S_v = \frac{d(vw_v)}{dx} \quad (12)$$

where

$p_v(x)$ = pressure of the vapor

$v(x)$ = velocity of the vapor

$A_v(x)$ = cross sectional area of vapor element
 $= \pi R(x)^2$

$S_v(x)$ = perimeter of vapor element
 $= 2\pi R(x)$

Expanding the right hand side of Equation (12), and using Equation (9), gives the following equation for the vapor pressure gradient:

$$\frac{dp_v}{dx} = -2\rho_v v \frac{dv}{dx} - \frac{2v^2\rho_v}{R} \frac{dR}{dx} + \frac{2\tau_v}{R} \quad (13)$$

The first two terms in Equation (13) represent the momentum effects of the vapor while the last term represents the usual wall-friction effect.

The interfacial shear stress may be written

$$\tau_v = \frac{1}{2} f \rho_v v(x)^2 \quad (14)$$

For low condensate velocities, according to Bergelin, et al [11], the two-phase friction factor may be approximated by the friction factor used in smooth tubes. For simplicity, the assumption was therefore made that the effect of the liquid film on the condenser surface is negligible,

and that

$$f = \frac{\text{constant}}{R_e^a} \quad (15)$$

where

$$\begin{aligned} R_e &= \text{vapor Reynolds number} \\ &= \frac{2R(x)\rho_v v(x)}{\mu_v} \end{aligned}$$

The constant and the exponent in Equation (15) would, of course, depend on the Reynolds number range, and are readily available in heat transfer textbooks [13].

A more refined analysis could be performed, using the Lockhart-Martinelli correlation [12] for two-phase frictional pressure drop, but since the friction effects were considered to be small in this study, the refined analysis was not warranted.

The above system of equations can be reduced to two first-order nonlinear differential equations with unknowns $v(x)$ and $\delta(x)$.

$$\frac{dv}{dx} = \frac{2(R_o + x \sin\phi) (T_s - T_\infty)}{\rho_v \left[\frac{\delta(x)}{k_f} + \frac{t}{k_w} + \frac{1}{h} \right] h_{fg} R(x)^2} - \frac{2v(x)}{R(x)} \left[\sin\phi - \cos\phi \frac{d\delta}{dx} \right] \quad (16)$$

and

$$\frac{d\delta}{dx} = \tan\phi - \frac{\rho_v f v(x)^2 \left[\frac{P_1(x)}{R(x)} + \frac{P_2(x)}{2} \right] + \rho_v v(x) \left[\frac{\mu_f R(x)^2}{2\rho_f} - 2P_1(x) \frac{dv}{dx} \right]}{P_1(x) \cos\phi \left[\rho_f \omega^2 R(x) + \frac{2\rho_v v(x)^2}{R(x)} \right]} \quad (17)$$

where

$$P_1(x) = (R_o + x \sin\phi) \frac{\delta(x)^3}{3} - \frac{5}{24} \cos\phi \delta(x)^4$$

$$P_2(x) = (R_o + x \sin\phi) \frac{\delta(x)^2}{2} - \cos\phi \frac{\delta(x)^3}{3}$$

A Runge Kutta numerical integration was used to solve these equations with an IBM 360 digital computer. It was hoped that by using two first order differential equations rather than a single second order equation as Daley did, that the sensitivity to the initial value of δ would be reduced. The integration was started by assuming initial conditions, $\delta = \delta_i$ and $v = 0$ at $x = 0$. With these initial conditions $\frac{d\delta}{dx} = \tan\phi$ at $x=0$. Figure 5 is a schematic drawing representing the calculated $\delta(x)$ for different initial values δ_i . Note that if δ_i is too small the calculated δ becomes negative before the condenser overfall (physically impossible solution). If δ_i is too large the calculated δ grows at a constant slope equal to $\tan\phi$ (physically unrealistic). With the proper choice of δ_i the calculated δ reaches a maximum along the length of the condenser and then tapers off to a value close to zero at the overfall. The exact value of δ at the overfall is not known. It was observed however that the calculated value of δ at the overfall was approximately 0.1 of δ_i , and the heat transfer rate was insensitive to an exact value at the overfall. This result agrees with Nimmo and Leppert [14] who experimentally found for laminar film condensation on a finite horizontal surface (with proper overfall drainage) that the heat transfer rates were practically independent of the end conditions.

Newton obtained results for half-cone angles of 0° , 0.1° , 0.2° and 0.3° . As the half-cone angle increased, the solution of the differential equations became extremely sensitive to the initial values of δ_i . He also noted that his results for $\delta(x)$ showed that (except near the ends of the condenser) $\frac{d\delta}{dx} \ll \tan\phi$. Newton, therefore, made this approximation, and simplified the model further using an order of magnitude analysis of the terms in Eqs. (16)

and (17). With these simplifications, Eqs. (16) and (17) were reduced to:

$$\frac{dv}{dx} = \frac{2(R_0 + x \sin \phi) (T_s - T_\infty)}{\rho_v \left[\frac{\delta(x)}{k_f} + \frac{t}{k_w} + \frac{1}{h} \right] r_g R(x)^2} - \frac{2v(x) \sin \phi}{R(x)} \quad (18)$$

and

$$\frac{\delta(x)^3}{3} R(x) \sin \phi (\rho_f \omega^2 R(x) + 2\rho_v v(x)^2) - \frac{\delta(x)^2}{4} \rho_v f v(x)^2 R(x) - \rho_v v(x) \frac{\mu_f R(x)^2}{2\rho_f} = 0 \quad (19)$$

Equation (18) was numerically integrated using the initial condition that $\delta_f = 0$ and $v = 0$ at $x = 0$, and using the cubic equation for $\delta(x)$, Equation (19). After the integration was completed for $\delta(x)$ and $v(x)$, then the energy equation was integrated over the length of the condenser to find the total heat transfer rate of the heat pipe. Newton's results for both Equations (16) and (17) and also for Equations (18) and (19) are tabulated in Table I.

Table I
Total Condenser Heat Flow Rate q (BTU/hr)

ϕ	Sol'n. to Equations (16) & (17)	Sol'n. to Equations (18) & (19)
0°	8,505	—
0.1°	10,082	9,836
0.2°	11,173	11,033
0.3°	11,904	11,769

Notice that the approximate solution is slightly conservative, and becomes more accurate as the half-cone angle increases. Since most practical designs will involve half-cone angles at least as large as 0.5° to 1.0°, the approximate solution can, therefore, be used with little error.

2.3 HEAT PIPE PARAMETRIC STUDY

A parametric study of the heat pipe operating characteristics was performed using this approximate solution [15]. In an attempt to establish these parametric relationships, a preliminary dimensional analysis was performed on the system of approximate equations which led to the functional relation

$$\frac{q}{k_f L (T_s - T_\infty)} = f \left(\frac{L \sin \phi}{R_o}, \frac{\omega R_o^2}{\nu_f}, \frac{k_w}{k_f}, \frac{t}{R_o}, \frac{h R_o}{k_f}, \frac{\rho_v \mu_v}{\rho_f \mu_f}, \frac{P_r}{c_p \Delta T / h_{fg}}, \frac{\mu_v}{\rho_f R_o \sqrt{h_{fg}}} \right) \quad (20)$$

where $\frac{q}{k_f L (T_s - T_\infty)}$ is a non-dimensional form of the heat transfer rate of the heat pipe. The independent operational variables were separated into broad categories of (1) working fluid properties, (2) operating conditions, and (3) heat pipe geometry. From these categories convenient parameters were selected to be studied.

Woodard [15] obtained results for a stainless steel heat pipe, with a 1/16 inch thick condenser wall, 9 inches long. Working fluids were water, ethyl alcohol and freon 113; condenser half-cone angles were 0°, 1°, 2° and 3°; condenser minimum internal radii were 0.125", 0.25", 0.5", 0.75", 1.0" and 2.0"; RPM was varied in increments of 600 RPM from 600 to 3600 RPM and values for the exterior heat transfer coefficient were 50, 100, 500, 1000, 3000 and ∞. The complete results are contained in Woodard's thesis [15].

Effect of Working Fluid

Figure 6 shows the heat transfer response of the rotating heat pipe to the overall physical properties of the working fluid in use. Water,

in the range of operation studied, is obviously the most satisfactory fluid. Its high latent heat of vaporization and high thermal conductivity relative to that of ethyl alcohol and freon 113, would explain this difference. For each working fluid, the heat transfer performance is improved with heat pipe operating temperature (and pressure).

Effect of Rotational Speed

Ballback's analysis indicated that the heat transfer capability of the heat pipe is proportional to the square root of the RPM. This behavior is weakened in Newton's analysis by the additional thermal resistance due to the condenser wall and the external heat transfer coefficient. However, analysis of the trend presented in Figure 7 indicates that the heat pipe response approaches this theoretical relationship, $q \propto \sqrt{\omega}$ as the exterior heat transfer coefficient becomes very, very large.

Effect of Exterior Heat Transfer Coefficient

Figures 7 & 8 suggest the dependence of the heat pipe capability on the condenser cooling mechanism. It is easily seen that the exterior heat transfer coefficient dominates the heat pipe capability when the exterior heat transfer mechanism is poor.

Effect of Heat Pipe Geometry

Figure 9 shows that the heat transfer rate increases rapidly with increasing half cone angle, from 0° to 1° , for a nominal RPM and heat transfer coefficient. This behavior then approaches an approximately linear response to half cone angles of 3 degrees. Figure 9 also shows that there is a significant heat transfer rate even when there is no internal taper to the condenser (when $\phi = 0^\circ$).

The change of heat transfer capability with change in internal radius is illustrated by Figure 10. The behavior of the heat transfer rate is related to the radius by two mechanisms, the change in condenser area and the change in centrifugal acceleration at the condensate film.

2.4 SUMMARY OF ANALYTICAL RESULTS

1. The approximate numerical solution [using Equations (18) and (19)] is valid for most practical heat pipe geometries.
2. In the temperature range from 80°F to 240°F, water appears to be the best working fluid.
3. The heat transfer capability of the heat pipe is dominated by the exterior heat transfer mechanism when this mechanism leads to low exterior heat transfer coefficients.
4. There is a significant condenser heat transfer rate even with a 0° half cone angle heat pipe. After an initial rapid rise with half cone angles from 0° to 1°, the heat transfer rate continues to increase approximately linearly with increasing half cone angles.
5. The heat transfer rate of the heat pipe approaches a function of the square root of RPM for efficient exterior heat removal mechanisms.
6. A change in the minimum internal condenser radius, R_0 has a large effect on heat pipe heat transfer.

3. EXPERIMENTAL PROGRAM

3.1 DESCRIPTION OF EQUIPMENT

The main components of the rotating, non-capillary heat pipe are grouped into the evaporator, condenser, auxiliary equipment, and instrumentation. Figure 11 is a schematic diagram of the test apparatus. A cross-sectional drawing of the assembled heat pipe is pictured in Figure 12, and Figure 13 is a photograph of the experimental facility.

Evaporator

The evaporator is a 3.125-inch inside diameter stainless steel cylinder, 5.90-inches long. One end is flanged to an outside diameter of 5.906-inches to accommodate the condenser and to support a large, single row precision ball bearing. The other end is flanged to an outside diameter of 4.50-inches to accommodate two pyrex glass end windows. The inner glass window is fused to a 1/4-inch diameter glass filling tube which passes through a hole in the outer window. The inner window presses against a neoprene o-ring and is separated from the outer window by a compressed fiber gasket. Both windows are held in place by a stainless steel end cap. (See Fig. 12.)

The evaporator is helically wound with an 11-gage Chromel-A heater wire in a 3/16-inch outside diameter Inconel sheath. The heater coils are bonded in place using a gold-nickel brazing alloy in a controlled hydrogen atmosphere. They are coated with a thin layer of Sauereisen cement and are packed with asbestos insulation to reduce radial heat losses. In addition, a 1/16-inch wide radial groove is machined into

the evaporator wall on either end of the heater element to reduce axial heat losses. Electrical power to the heater is passed by a graphite brush assembly through bronze collector rings. Power is furnished to the heater coils by a 120 volt DC motor generator set with an automatically regulated voltage output, and is controlled using five resistive load banks in series with the heater coils.

Condenser

The condenser is a 10.0-inch long stainless steel, truncated cone with a 1.0 degree half-cone angle and with a 1/16-inch wall thickness. The large end of the condenser is flanged to bolt to the evaporator and has an inside diameter of 1.81-inches. The small end is machined into a cylinder 1.46-inches inside diameter, by 1.50-inches long. It is flanged to accommodate a cylindrical end plug. Each flanged joint is sealed with a teflon-coated, metallic o-ring.

The stainless steel condenser end plug is hollowed out to allow the pressure transducer arm to be passed through its inside face, and to allow the drive shaft to be threaded and keyed in place. The outer end of the plug is machined down to four flat sides, each 7/8-inch wide and 7/8-inch long to accommodate phenolic thermocouple junction boards.

Auxiliary Equipment

The auxiliary equipment are grouped into the drive assembly, test stand, spray cooling assembly, safety shields, and filling system.

Drive Assembly

The drive assembly consists of the drive shaft, support bearing, pulley and variable drive motor. The drive shaft is a 3/4-inch diameter stainless steel cylinder which is hollowed out to allow the instrumentation

leads to be connected to the slip-ring unit. The outside diameter of the shaft is stepped in several places to thread into the condenser end plug, to accommodate a 2.65-inch diameter drive pulley, and to support a double row, angular contact bearing. Each end of the shaft is internally threaded. The pressure transducer arm is screwed into one end and the slip-ring coupling into the other. The shaft is screwed securely into the condenser end plug and is keyed in place. Torque is applied to the shaft by a V-belt using a 2HP, 3 phase variable speed motor. The motor is capable of speeds from 450 to 4500 RPM and is equipped with a magnetic disc brake and an electric remote control unit.

Test Stand

The test stand is designed so that the heat pipe can be rigidly supported with its longitudinal axis ranging in position from 0 to 90 degrees from the horizontal. Both the heat pipe and variable drive motor are mounted on steel bed-plates connected by a 4-inch diameter iron pipe. The iron pipe is held in place by three 2-inch thick clamps which are supported two feet off the ground by a 1/4 inch steel plate. As the heat pipe is rotated in any position, the drive motor rotates with it and the entire assembly is then securely held in place.

Spray Cooling Assembly

Cooling of the condenser section is done by spraying tap water on the outside of the condenser during rotation. The condenser section is enclosed by a 9-inch long 13-inch diameter well-insulated stainless steel cylinder. The ends of this cylinder have Garlock rubber seals separating them from the rotating condenser section. The condenser cover is slid into place over the condenser section through its open ends and is then bolted

in place to the support plate. The cover has an 8-inch x 6-inch door on it to make adjustments or repairs on the heat pipe without removing the entire cover. The cover has eight spray nozzles. Each nozzle is mounted at the same axial position but is spaced 45° apart on the circumference. Various nozzles may be used to give a range of water droplet sizes from 300 to 600 microns. The cooling water flows from copper feed lines to a mixing tube soldered onto the top of the condenser cover. The coolant flows from the mixing tube through insulated plastic tubing to each of the spray nozzles. It drains from the bottom of the condenser cover to another mixing tube before being dumped into the building drain lines.

Safety Shields

To insure safe operation, the entire heat pipe assembly is surrounded by 1/8 inch thick stainless steel shielding which easily bolts to the support plate.

Filling System

The filling system consists of a glass filling manifold, mercury manometer and vacuum system. The glass manifold and manometer are shown schematically in Figure 14. A mechanical vacuum pump and air-cooled oil diffusion pump are used to evacuate the system.

Instrumentation

Temperature Measurements

Eight Kapton insulated copper-constantan thermocouples are used on the rotating heat pipe. Four thermocouples are manufactured with a 1/16 inch diameter stainless steel sheath. Each of these is placed within a

1/16 inch diameter well drilled 3 1/2 inches deep into the evaporator wall at different radial positions to monitor the radial heat transfer into the evaporator. One thermocouple is located 0.066 inch radially outward from the inside of the evaporator surface; another is located 0.188 inch radially outward; the remaining two are each located 0.125 inch radially outward, but are spaced circumferentially 180° apart to monitor temperature uniformity. Each radial location has an estimated uncertainty of ± 0.005 inches. Two thermocouples, sealed in stainless steel sheaths, are suspended in the evaporator vapor space to measure the saturation temperature of the vapor. Two additional thermocouples are spot welded to the outside of the condenser at different axial positions to monitor the heat transfer through the condenser. The leads from all these thermocouples are brought along the sides of the condenser and through the small rear condenser flange to the phenolic junction boards on the condenser end plug. From the junction boards, the leads go inside the shaft to a mercury slip-ring unit, rated at less than 10 micro-volts noise at speeds to 4000 RPM. The slip-ring output is fed to a Hewlett-Packard 2010C Data Acquisition System which has an accuracy of ± 0.5 microvolts.

All evaporator wall thermocouples were calibrated with an uncertainty of $\pm 0.5^\circ\text{F}$ using the triple point of water (32.0°F), the boiling point of water (212.0°F at 14.696 psia), the melting point of tin (449.4°F), and the melting point of lead (621.3°F). The other thermocouples were calibrated with an uncertainty of $\pm 0.2^\circ\text{F}$ using the triple point and the boiling point of water.

The temperature of the condenser cooling water is measured before and after spraying the test section by quartz crystal thermometers mounted in

well-insulated mixing tubes located above and below the condenser spray cooling cylinder. These thermometers have an accuracy of better than $\pm 0.1^\circ\text{F}$.

Pressure Measurements

The saturation pressure of the vapor is measured by a semi-conductor pressure transducer mounted in the vapor space at the small end of the condenser. The transducer is threaded on a 1/4-inch diameter, 2-inch long arm which extends from the shaft through the end plug and into the vapor space. The leads of the probe pass through the transducer arm, through the shaft to the junction boards, and out to the slip-ring unit.

The pressure transducer was calibrated against a Wallace-Tiernan standard pressure gage (with an accuracy of 0.03 ± 0.01 psia) for pressures greater than atmospheric, and against a mercury manometer (with an uncertainty of ± 0.02 psia) for pressures less than atmospheric. The calibration was performed at different operating temperatures by placing the transducer within a controlled temperature oven with a quartz crystal thermometer.

Coolant Flow Rate Measurements

The coolant flow rate is measured by passing the coolant through a calibrated flow rotameter (with an accuracy of $\pm 2\%$) before it enters the spray nozzles.

Rotational Speed Measurements

The rotational speed of the heat pipe is measured using a geared fly-wheel and a variable reluctance transducer whose output frequency is recorded using a Systron counter. An electronic strobe light is used as a check.

Electrical Power Measurements

Electrical power to the heater coils is measured by an ammeter and voltmeter.

3.2 EXPERIMENTAL PROCEDURES

The experimental procedures consist of cleaning and filling procedures and operational procedures.

Cleaning and Filling Procedures

In order to obtain film condensation in the heat pipe condenser when water was the working fluid, the interior surface was prepared to insure that proper wetting occurred. In addition to wetting, it was desirable to remove as much of the non-condensable gases which were present, and to fill the heat pipe with the same amount of fluid each time. The above goals were accomplished by performing a detailed cleaning and filling procedure as described below.

- a. The heat pipe was placed in the vertical position and mounted to the fill equipment.
- b. With end windows and "O" rings removed, the heat pipe was filled with a chlorinated hydrocarbon degreasing compound such as Trichloroethylene.
- c. The pipe was then drained and filled with distilled water.
- d. Steps b. and c. were repeated.
- e. The pipe was then flushed three times with alcohol.
- f. Step c. was repeated.
- g. The pipe was filled with a warm mixture of 8 parts distilled

water, 2 parts ethyl alcohol, 2 parts 50% NaOH solution and 1/2 part 30% H_2O_2 solution.

h. It was then thoroughly rinsed with distilled water, while noting any signs of non-wetting.

i. The pipe was kept filled with water until ready for filling.

When the heat pipe was ready to be filled, it was prepared in the following manner.

a. All the water was drained from the pipe, and the end windows were mounted in place.

b. The glass filling tube was connected to the filling manifold, and a vacuum was pulled on the test section for about 1/2 hour.

c. Approximately 150 ml. of de-gassed, distilled water was then slowly bled into the heat pipe.

d. The glass fill tube was then sealed under vacuum.

Operational Procedure

Having completed the filling procedure, the heat pipe was ready to run at a pre-determined RPM. About 10 drops of lubricating oil were added to the oil fill tube at the top of the large bearing. The cooling water lines were turned on so that the rotameter was at approximately 30% flow. The drive motor was turned on and the heat pipe was slowly brought up to the desired RPM. Once a liquid annulus was formed in the evaporator and the desired RPM was reached, the DC motor generator was turned on and power was added to the evaporator. After thermal equilibrium was reached for a particular power setting, data was taken by the instrumentation described earlier. Shut-down was accomplished by first shutting off the current to the heater, and then decreasing the RPM by use of the remote control unit.

3.3 REDUCTION OF DATA

The condenser heat transfer rate was experimentally determined using the measured mass rate of flow and the overall temperature increase of the cooling water in Equation (21).

$$q = wc_p \Delta T \quad (21)$$

A correction was made to this result, however, to take into account frictional heating effects of the bearings and seals, and viscous dissipation effects within the cooling water during rotation. To measure these effects the heat pipe was rotated at various rotational speeds with cooling water flowing through the spray nozzles, but with no input power applied to the evaporator. In each case, the mass rate of flow of the cooling water was measured along with the overall temperature increase of the cooling water across the condenser box. These measured values were used in Equation (21) to calculate the heat removed due to frictional effects at various rotational speeds. This calculated frictional heat transfer rate was subsequently subtracted from the total condenser heat transfer rate for each selected rotational speed.

4. EXPERIMENTAL RESULTS

4.1 EVAPORATOR PERFORMANCE

During the initial operating runs, the evaporator performance was studied using visual observations and the measured evaporator wall temperature profile. It was noted, for instance, that at high rotational speeds, the number of active nucleation sites decreased and bubble departure diameters were smaller. This result agrees with the observations of Gray & Marto [16, 17] during nucleate boiling within a cylindrical, rotating boiler. In addition, at low saturation pressures (corresponding to low input powers), the nucleate boiling action was violent, with large vapor bubbles and a frothy liquid-vapor interface. On the other hand, at high saturation pressures, the boiling action was more controlled, with smaller bubbles.

Temperature and pressure data were recorded, and the measured temperature within the vapor space compared to within 1°F of the saturation temperature calculated from the measured vapor pressure. Moisture within the pressure transducer, however, prevented its further use due to unpredictable shifts in its zero reading.

Using the measured radial wall temperature profile in the evaporator, and assuming one-dimensional conduction, the heat flux and the inside wall surface temperature were calculated at the axial midpoint of the evaporator. Figure 15 presents the calculated heat flux versus $(T_w - T_s)$ for a 700 RPM run (corresponding to 22 G's at the test surface). Notice that as the saturation temperature in the vapor space T_s increases, due to an increase

in the operating pressure with applied power input, the wall superheat decreases. The heat transfer coefficient therefore increases with applied heat load and operating pressure. This result is in agreement with the well-known pressure effect upon saturated nucleate pool boiling [13]. The data of Ponter & Haigh [18] at 1G, which shows this pressure effect, is plotted in Figure 15. In addition, the data of Gray, Marto & Joslyn [16], at 25 G's is shown for comparison. The first six experimental data points are in reasonable agreement with the other investigations. Data point 7 however, appears to be in error, perhaps due to the large uncertainty in the extrapolated inside wall surface temperature at high power inputs.

4.2 CONDENSER PERFORMANCE

A great deal of difficulty was initially experienced in trying to obtain good wetting of the condensate upon the stainless steel condenser surface [10]. The poor wettability of the condensate led to break-up of the condensate film with rivulet formation. After attempting several unsuccessful cleaning procedures, the one described above was tried and good wetting was obtained. The condensate then appeared as a mirror smooth film on the inside of the condenser surface. No ripples, rivulets or waves were observed.

Effect of Dropwise Condensation

Figure 16 compares the condenser heat transfer results at two rotational speeds of 700 and 2100 RPM. The heat transfer rate was calculated from the measured mass rate of flow of the cooling water, together with the measured temperature increase across the coolant mixing box, as noted earlier. Data

was taken during smooth film condensation (with good wetting) and also with dropwise condensation (with poor wetting). The dropwise condensation mode was promoted by wiping the inside of the condenser surface with an oily cloth. From this data, it is evident that the performance of the condenser can be improved with higher RPM, and with dropwise condensation. Note, however, that the influence of rotational speed is felt more strongly in the film condensation mode than in the dropwise condensation mode. The effect of high centrifugal acceleration may tend to flatten out the condensate drops, rendering them less effective in their mechanism of heat removal. This behavior (i.e. the influence of high centrifugal acceleration upon dropwise condensation) should therefore receive further study. Also, at a given RPM, it appears that the increase in the heat transfer capability of the heat pipe in going from film condensation to dropwise condensation is more pronounced at lower saturation temperatures, corresponding to lower operating pressures. This behavior also warrants additional study.

Effect of Non-Condensable Gases

In Figure 17, the heat pipe condenser performance is compared for two different filling procedures. For Run 1, the heat pipe was evacuated for 10 minutes to 19 mm Hg before filling and sealing. On the other hand, for Run 3, the heat pipe was evacuated for 30 minutes to 4.5 mm Hg prior to filling and sealing. The difference in behavior for these two runs is therefore due to varying amounts of non-condensable gas trapped within the heat pipe. Film condensation occurred during both runs. Notice that at 700 RPM, as well as 2100 RPM, better performance occurred during Run 3 which presumably had a smaller amount of non-condensable gas present. This result agrees with the well-known influence of non-condensable gases on condensation heat

transfer [13]. In general, the non-condensable gases blanket the condenser surface and prevent the migration of the vapor molecules toward this cold surface, reducing the heat transfer. In a conventional, capillary-wick heat pipe (with no rotation) the vapor movement pushes all the non-condensable gases down to the far end of the condenser where a vapor-gas interface may exist. This interface is not sharp however because of diffusion effects of the gas molecules through the vapor [19]. In addition, gravitational effects may also lengthen this interface. Within the rotating heat pipe, the centrifugal acceleration may force the heavier non-condensable gas (air) toward the evaporator, spreading out the vapor-gas interface along the entire condenser surface. Such an effect should be more important at low operating pressures where the steam density is very small compared to the density of air (see Figure 17).

Condenser Surface Temperature Profiles

During Runs 1, 2 and 3 an unexpected longitudinal temperature gradient was measured on the condenser surface using the thermocouples mentioned earlier. A marked increase in condenser surface temperature occurred toward the evaporator section of the heat pipe. Additional copper-constantan thermocouples were therefore spot welded to the condenser surface to provide for a better temperature profile. Runs 4, 5, 6, and 7 were made while these more complete temperature profiles were measured. [20]. Figures 18 & 19 show these profiles for Run 4 at 700 and 2100 RPM and at different input powers. The exact cause of this non-uniform wall temperature is not known, however, this may be indicative of (a) non-condensable gases in the vapor space, (b) a poor coolant spray distribution upon the condenser surface (see Fig. 12), (c) a longitudinal heating effect

due to conduction from the electrical heater or from frictional heating in the large bearing and Garlock seal.

4.3 COMPARISON OF THEORY AND EXPERIMENT

Figures 20 through 23 compare the experimental heat transfer rates to the predicted theoretical rates. Some typical experimental error limits are included.

In arriving at the theoretical results, several modifications were made to Eqs.(11)&(18). Since the condenser wall surface temperature was measured during these runs, it was assumed to be known in the theoretical model. The outside surface heat transfer coefficient was an unknown and was therefore not used. Equation (18) was consequently modified as follows:

$$\frac{dv}{dx} = \frac{2(R_o + X\sin\phi) (T_s - T_w(x))}{\rho_v \left[\frac{\delta(x)}{k_f} + \frac{t}{k_w} \right] h_{fg} R(x)^2} - \frac{2v(x)\sin\phi}{R(x)} \quad (22)$$

Notice that the total thermal driving force becomes $T_s - T_w(x)$ and the total resistance includes the condensation resistance and the wall conduction resistance. The outside heat transfer resistance is unnecessary since $T_w(x)$ is known. Equation (11) was modified in a similar way.

To arrive at an analytical expression for $T_w(x)$, the measured wall temperature profiles (See Figures 18 and 19) were used. A cubic polynomial approximation to the data was made using a least squares technique [20]. The resulting cubic polynomial was used for $T_w(x)$ in Equation (22), and together with Equation (19), a numerical integration was performed. During the integration, condensate properties were evaluated at a film

temperature equal to the arithmetic average of the saturation temperature and the local inside wall temperature.

Figure 20 shows the comparison for Run 4 with water at 700 & 2800 RPM. The theoretical results are approximately 20 percent higher than the experimental data at 700 RPM, and about 10 percent higher at 2800 RPM. Such agreement is reasonable during film condensation heat transfer. Similar results are evident in Figure 21 for Run 5 with water. Figure 22 compares the theory to the experimental data for ethyl alcohol, and Figure 23 is for freon-113. Notice that for water, the theoretical results are higher than the experimental data, but for ethyl alcohol and freon, the theoretical results are less than the experimental data. This opposite trend was also recently found by Lee & Mital [21] during operation of a vertical, stationary closed thermosyphon. They found that their theory overestimates the heat transfer rate for water and underestimates the rate for freon-11. The reason for this discrepancy is not clear at this time. It may be due to differences in vapor densities between water, alcohol and freon 113, leading to differences in non-condensable gas migration, or to differences in vapor velocity effects within the theoretical model. In general, however, the agreement is reasonable and the approximate theory can be used to predict rotating heat pipe performance to within $\pm 20\%$.

5. CONCLUSIONS AND RECOMMENDATIONS

5.1 CONCLUSIONS

Based upon the experimental results obtained for the range of variables covered during this investigation, the following conclusions can be made:

1. The rotating, non-capillary heat pipe can be used effectively to transfer large quantities of heat in rotating systems. Its performance improves with higher internal pressures.
2. The approximate theoretical model developed during this work can be used to predict rotating heat pipe performance to within ± 20 percent.
3. The presence of non-condensable gases can seriously impair the heat transfer performance of these devices.
4. Dropwise condensation gives better performance than film condensation. This effect is more pronounced at lower pressures and rotational speeds.

5.2 RECOMMENDATIONS

It is recommended that:

1. Further work should be performed to improve upon the heat transfer characteristics of these devices, including a study of dropwise condensation during centrifugal acceleration.

2. In designing a rotating, non-capillary heat pipe, care should be taken to ensure that the outside heat transfer coefficient is sufficiently high. Otherwise, performance will be impaired.
3. A study should be performed on the migration and influence of non-condensable gases during rotating heat pipe operation.

BIBLIOGRAPHY

1. Gray, V. H., "The Rotating Heat Pipe - a Wickless Hollow Shaft for Transferring High Heat Fluxes", ASME Paper No. 69-HT-19, presented at the ASME-AIChE 11th National Heat Transfer Conference, Minneapolis, Minnesota, August, 1969.
2. Marto, P. J., Daley, T. J. and Ballback, L. J., "An Analytical and Experimental Investigation of Rotating, Non-Capillary Heat Pipes - Annual Report", NPS - 59MX70061A, June, 1970.
3. Ballback, L. J., "The Operation of a Rotating, Wickless Heat Pipe", M. S. Thesis, Naval Postgraduate School, Monterey, California, December, 1969.
4. Daley, T. J., "The Experimental Design and Operation of a Rotating, Wickless Heat Pipe", M. S. Thesis, Naval Postgraduate School, Monterey, California, June, 1970.
5. Sparrow, E. M. and Gregg, J. L., "A Theory of Rotating Condensation", Journal of Heat Transfer, 81, pp. 113-120, May, 1959.
6. Sparrow, E. M. and Hartnett, J. P., "Condensation on a Rotating Cone", Journal of Heat Transfer, 83, pp. 101-102, February, 1961.
7. Singer, R. M. and Preckshot, G. W., "The Condensation of Vapor on a Horizontal Rotating Cylinder", Proceedings of the Heat Transfer and Fluid Mechanics Institute, No. 14, p. 205, 1963.
8. Chato, J. C., "Condensation in a Variable Acceleration Field and the Condensing Thermosyphon", Journal of Engineering for Power, 87, pp. 355-360, October, 1965.
9. Dhir, V. and Lienhard, J., "Laminar Film Condensation on Plane and Axisymmetric Bodies in Non-uniform Gravity", Journal of Heat Transfer, 93, pp. 97-100, February, 1971.
10. Newton, W. H., "Performance Characteristics of Rotating, Non-Capillary Heat Pipes", M. S. Thesis, Naval Postgraduate School, Monterey, California, June, 1971.
11. Bergelin, O. P., Kegel, P. K., Carpenter, F. G., and Gayley, C., Heat Transfer and Fluid Mechanics Institute, Berkeley, California, 1949.
12. Lockhart, R. W. and Martinelli, R. C., "Proposed Correlation of Data for Isothermal Two-Phase Two Component Flow in Pipes", Chemical Engineering Progress, 45, p. 39, 1949.

13. Rohsenow, W. M. and Choi, H. Y., Heat, Mass, and Momentum Transfer Prentice-Hall, Inc., 1961.
14. Nimmo, B. and Leppert, G., "Laminar Film Condensation on a Finite Horizontal Surface", Heat Transfer 1970, Vol. VI, Elsevier Publishing Co., Amsterdam, 1970.
15. Woodard, J. S., "The Operation of Rotating, Non-Capillary Heat Pipes", M. S. Thesis, Naval Postgraduate School, Monterey, California, March, 1972.
16. Gray, V. H., Marto, P. J. and Joslyn, A. W., "Boiling Heat Transfer Coefficients, Interface Behavior, and Vapor Quality in Rotating Boiler Operating to 475 G's", NASA TN D-4136, March, 1968.
17. Marto, P. J. and Gray, V. H., "Effects of High Accelerations and Heat Fluxes on Nucleate Boiling of Water in an Axisymmetric Rotating Boiler", NASA TN D-6307, May, 1971.
18. Ponter, A. B. and Haigh, C. P., "Sound Emission and Heat Transfer in Low Pressure Pool Boiling", International Journal of Heat and Mass Transfer, 12, pp. 413-427, April, 1969.
19. Marcus, B. D., "Theory and Design of Variable Conductance Heat Pipes: Control Techniques", Research Report No. 2, TRW Systems Group, July, 1971.
20. Schafer, C. E., "Augmenting the Heat Transfer Performance of Rotating, Two Phase Thermosyphons", M. S. Thesis, Naval Postgraduate School, Monterey, California, December, 1972.
21. Lee, Y. and Mital, U., "A Two-Phase Closed Thermosyphon", International Journal of Heat and Mass Transfer, 15, pp. 1695-1708, September, 1972.

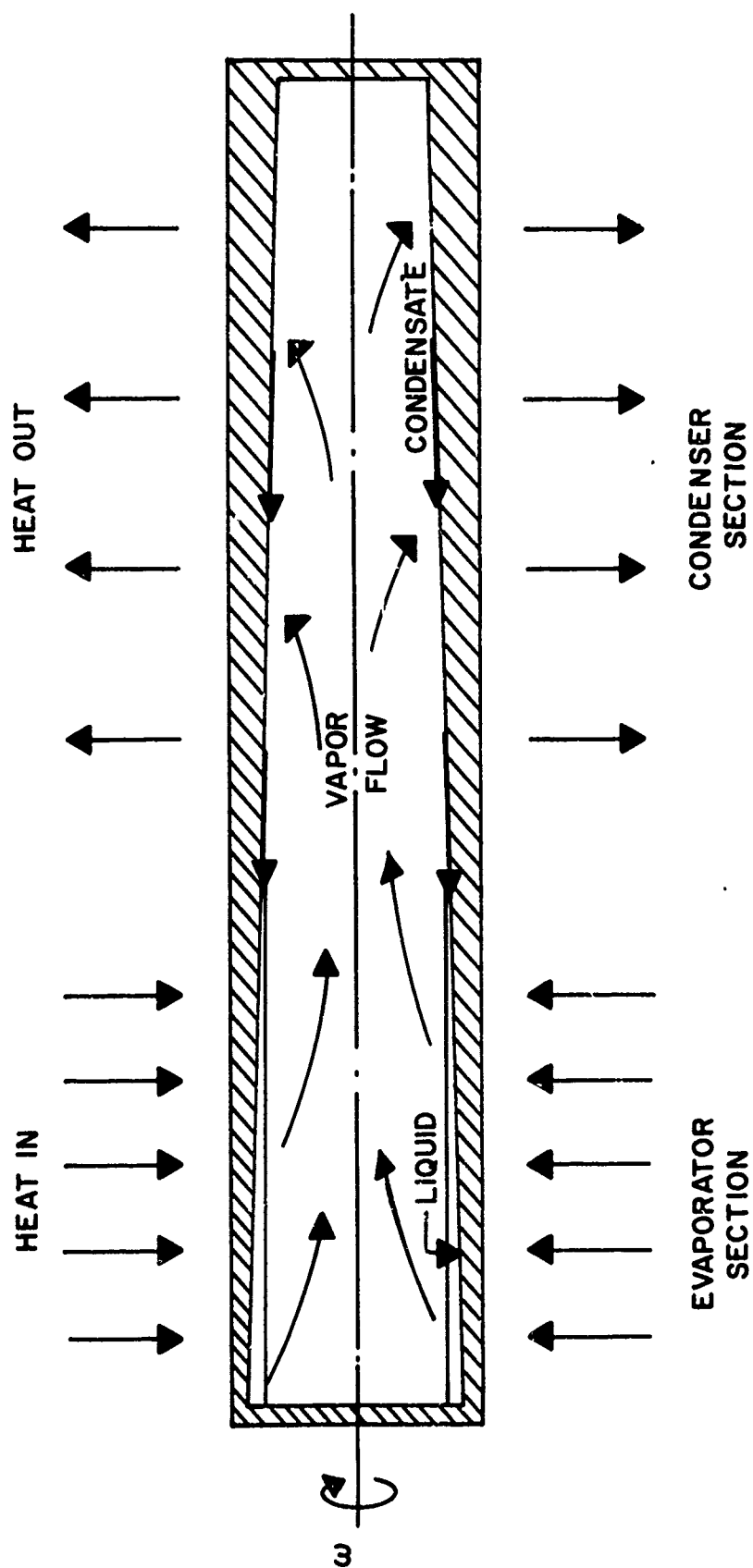


FIGURE 1 SCHEMATIC DRAWING OF ROTATING, NON-CAPILLARY HEAT PIPE

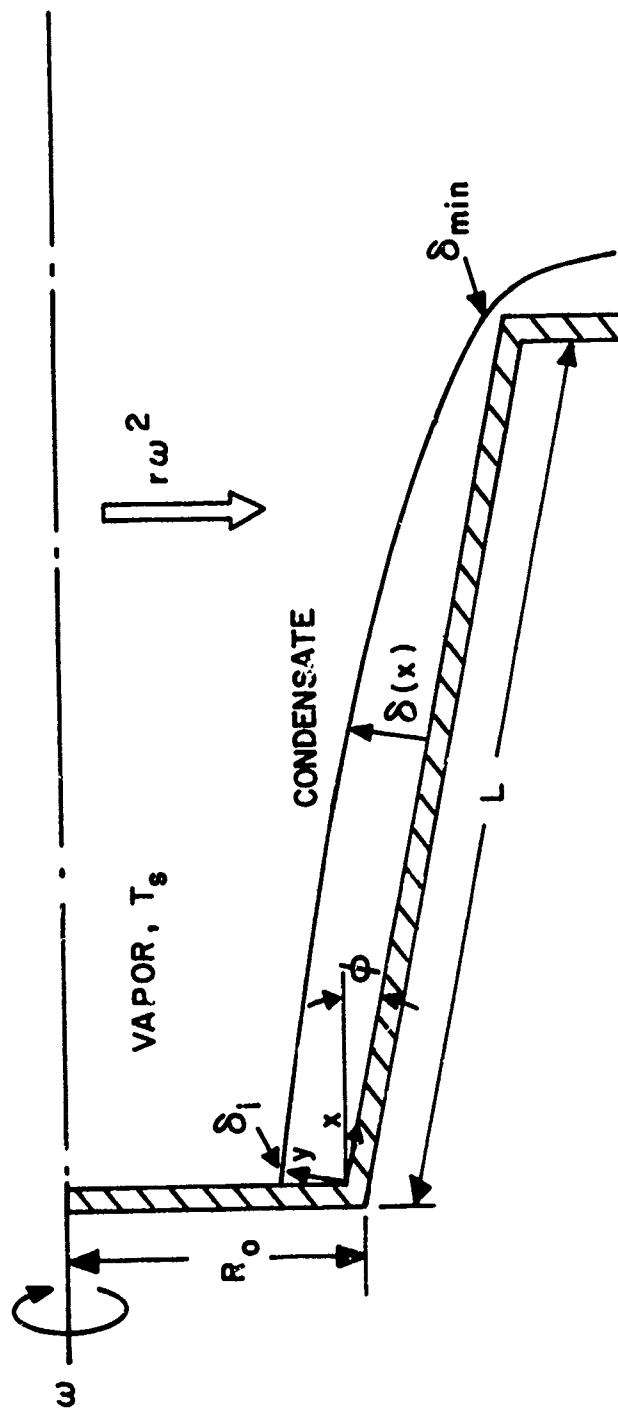


FIGURE 2 COORDINATE SYSTEM AND GEOMETRY FOR LAMINAR FILM CONDENSATION MODEL, SHOWING SCHEMATIC BEHAVIOR OF CONDENSATE FILM UNDER INFLUENCE OF ROTATIONAL ACCELERATION

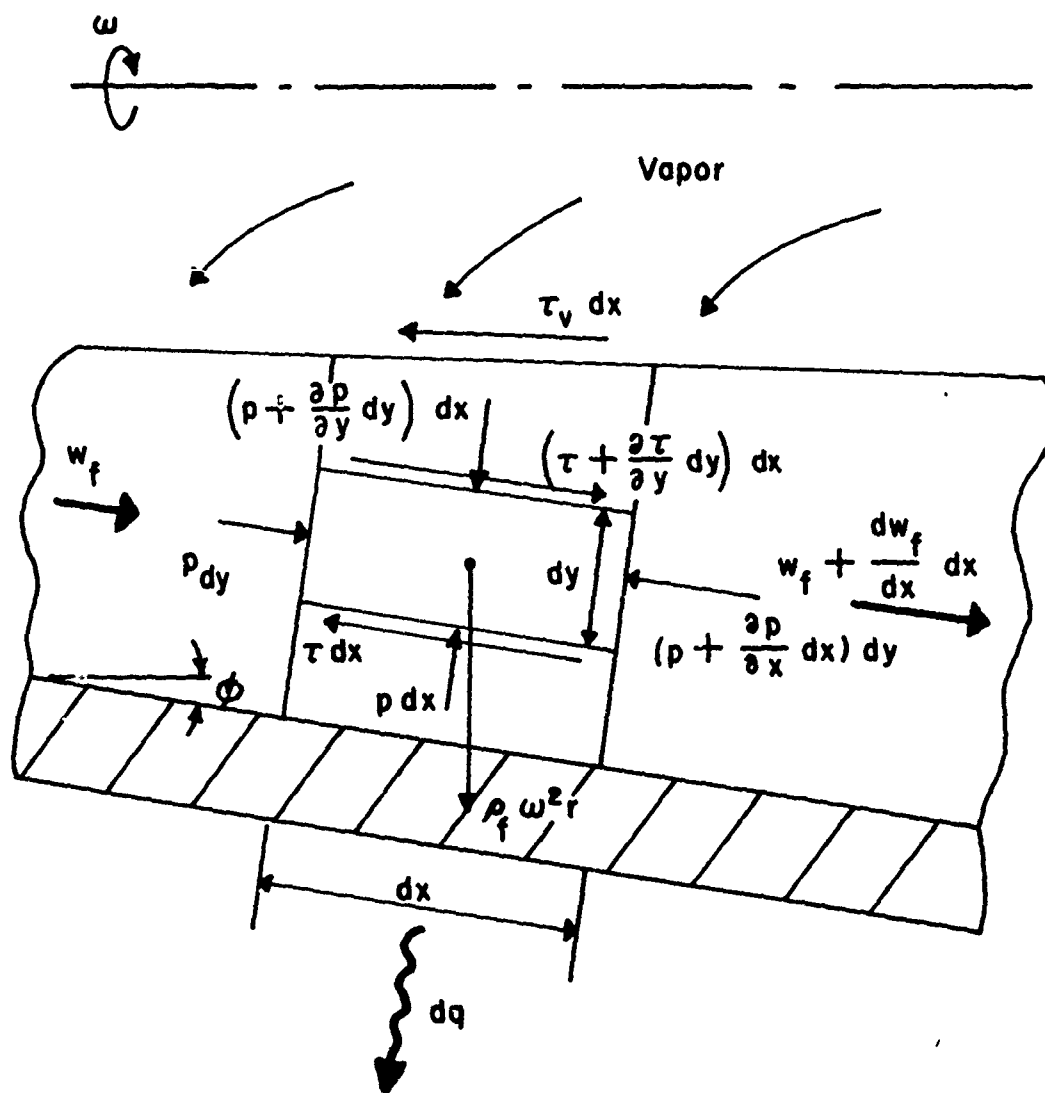


FIGURE 3 DIFFERENTIAL ELEMENT OF CONDENSATE FILM

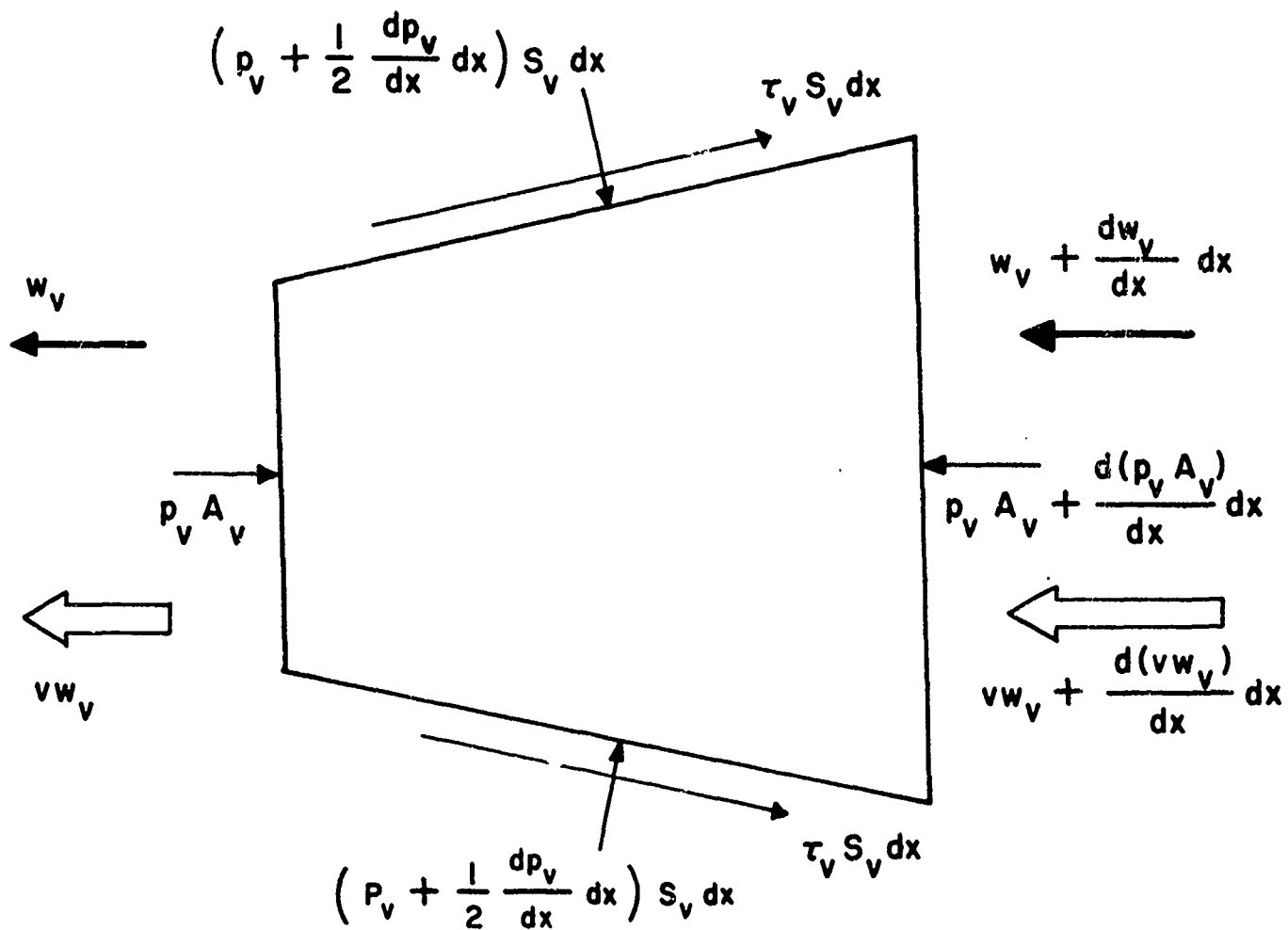


FIGURE 4 DIFFERENTIAL ELEMENT OF VAPOR CORE

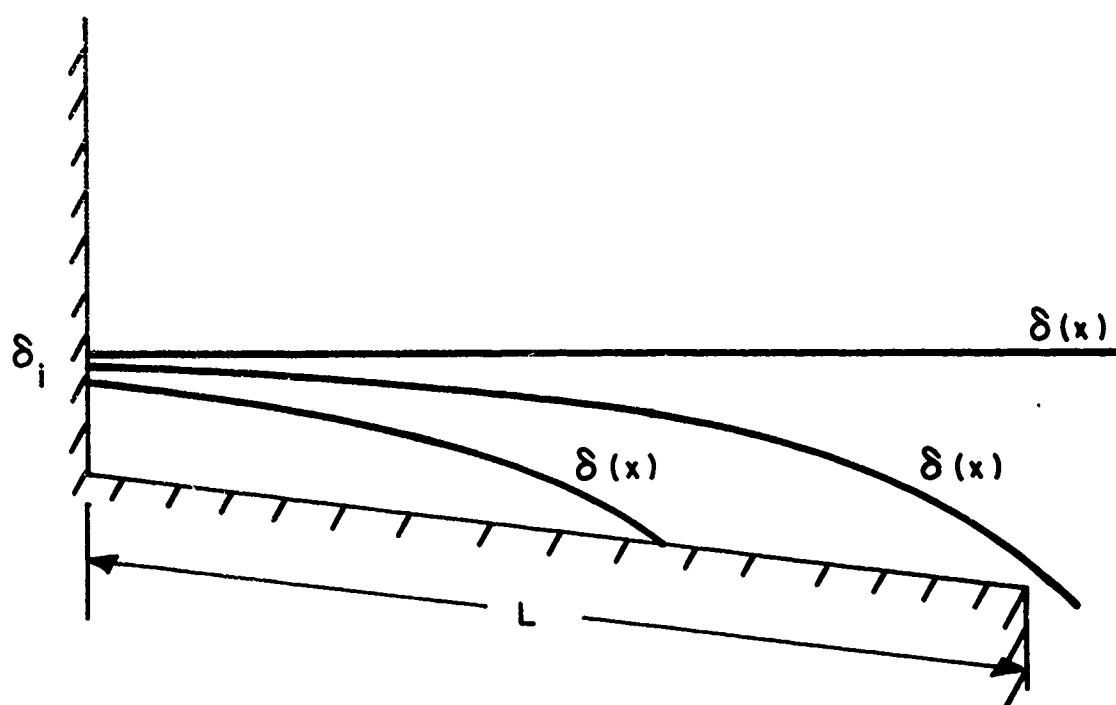


FIGURE 5 SCHEMATIC DIAGRAM OF CALCULATED FILM THICKNESS $\delta(x)$
FOR DIFFERENT INITIAL VALUES δ_i

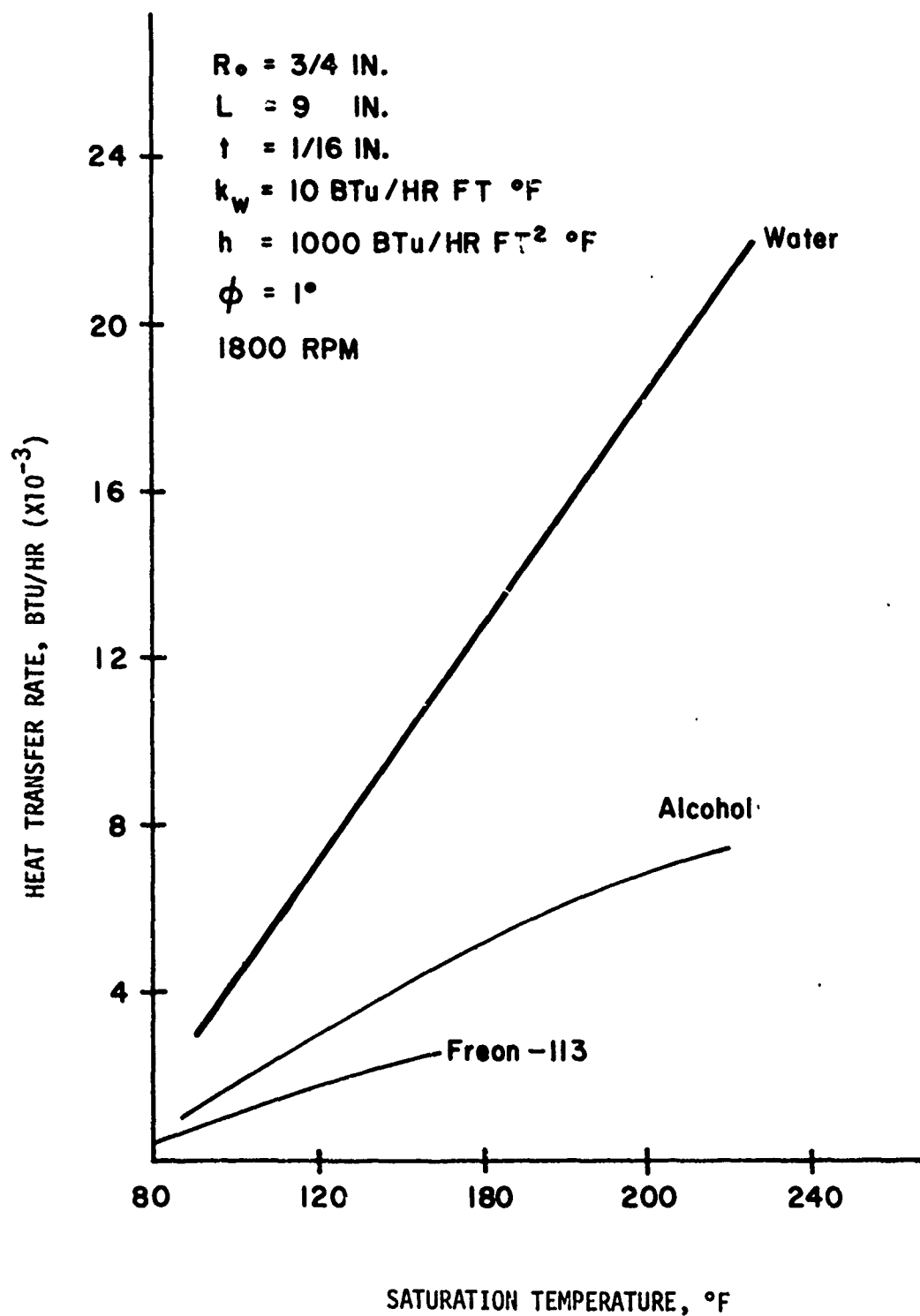


FIGURE 6 THEORETICAL HEAT TRANSFER RATE VS. SATURATION TEMPERATURE
FOR WATER, ALCOHOL, AND FREON-113

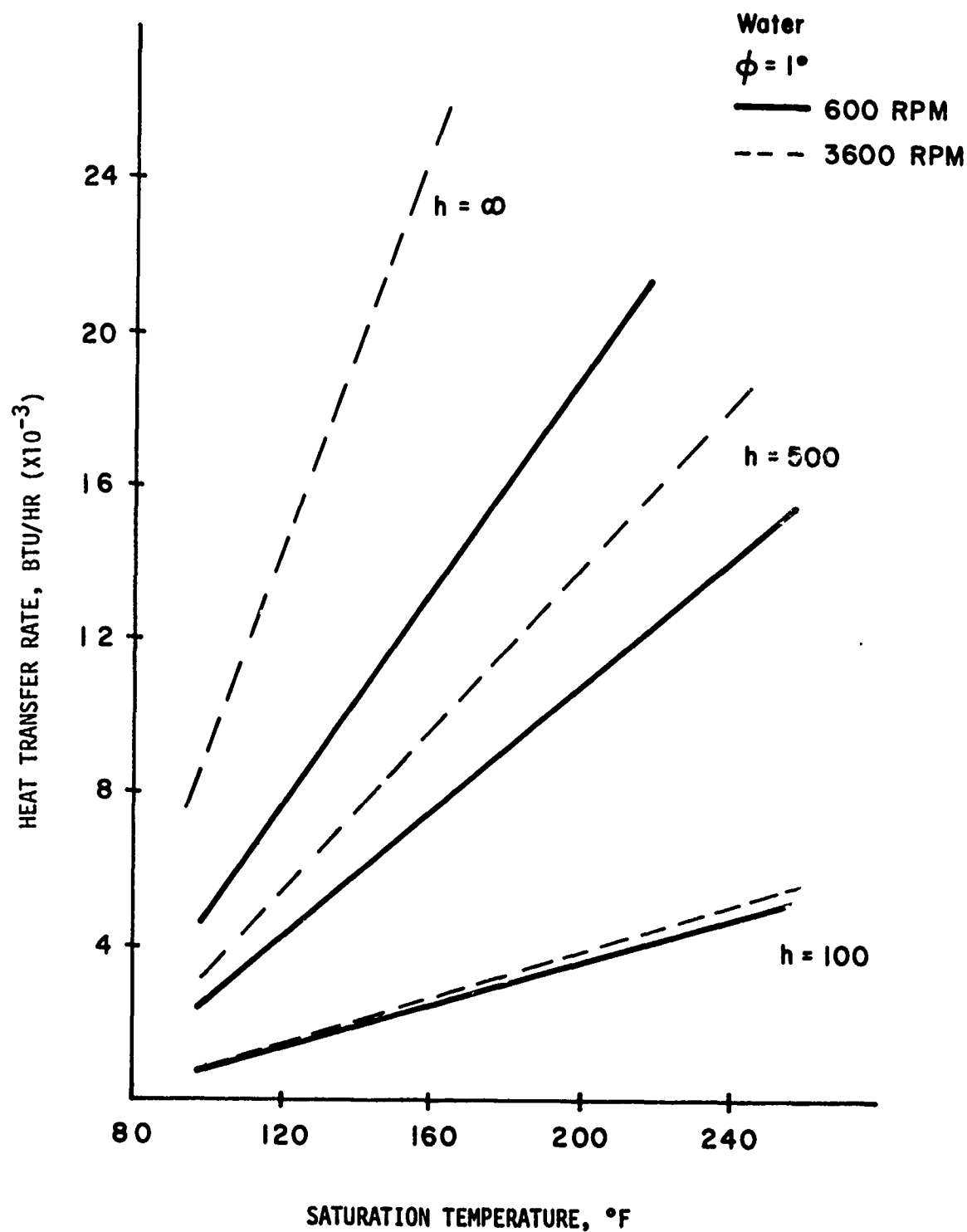


FIGURE 7 THEORETICAL HEAT TRANSFER RATE VS. SATURATION TEMPERATURE
FOR WATER SHOWING INFLUENCE OF RPM

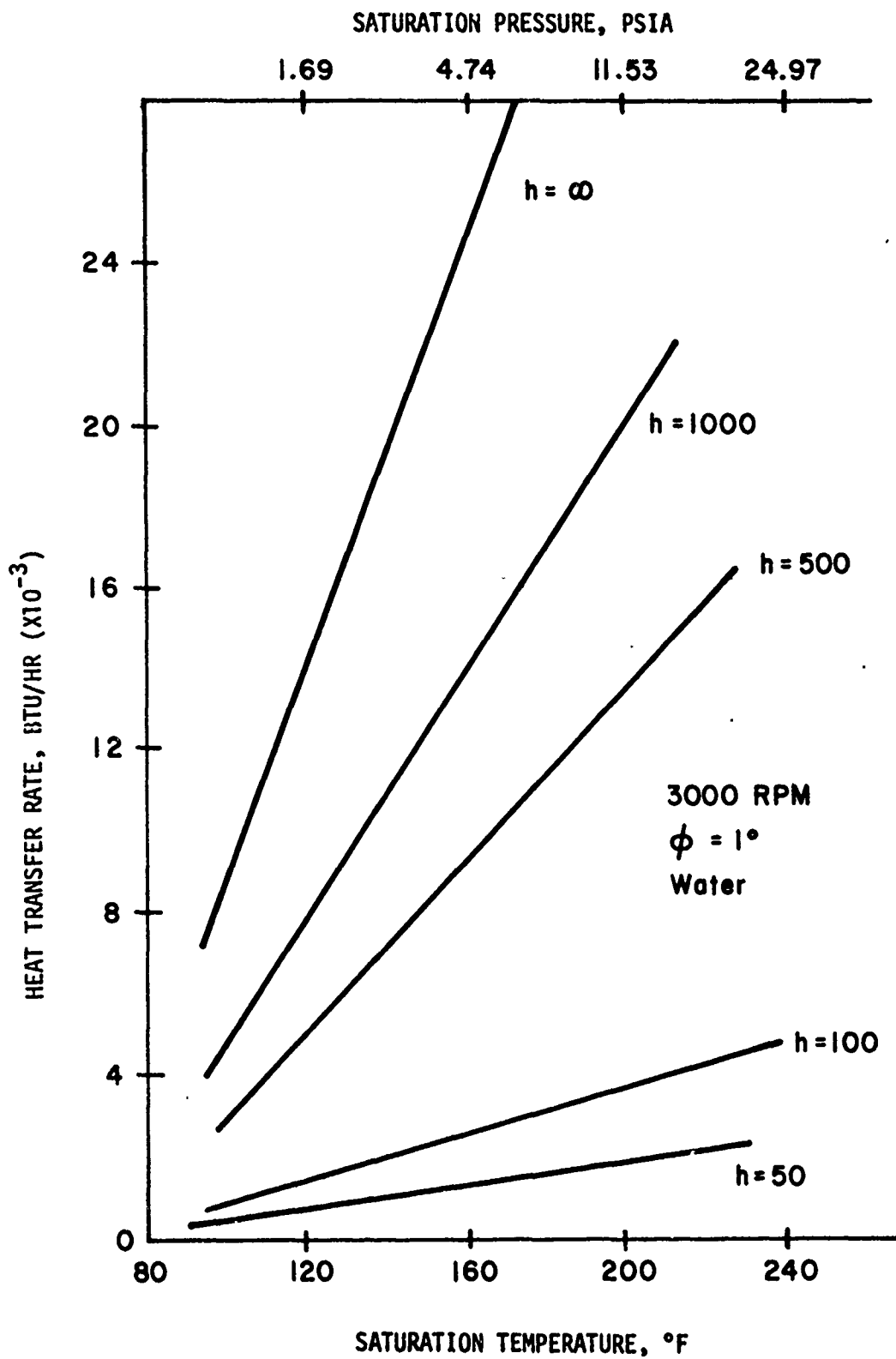


FIGURE 8 THEORETICAL HEAT TRANSFER RATE VS. SATURATION TEMPERATURE
 FOR WATER SHOWING INFLUENCE OF EXTERNAL HEAT TRANSFER COEFFICIENT

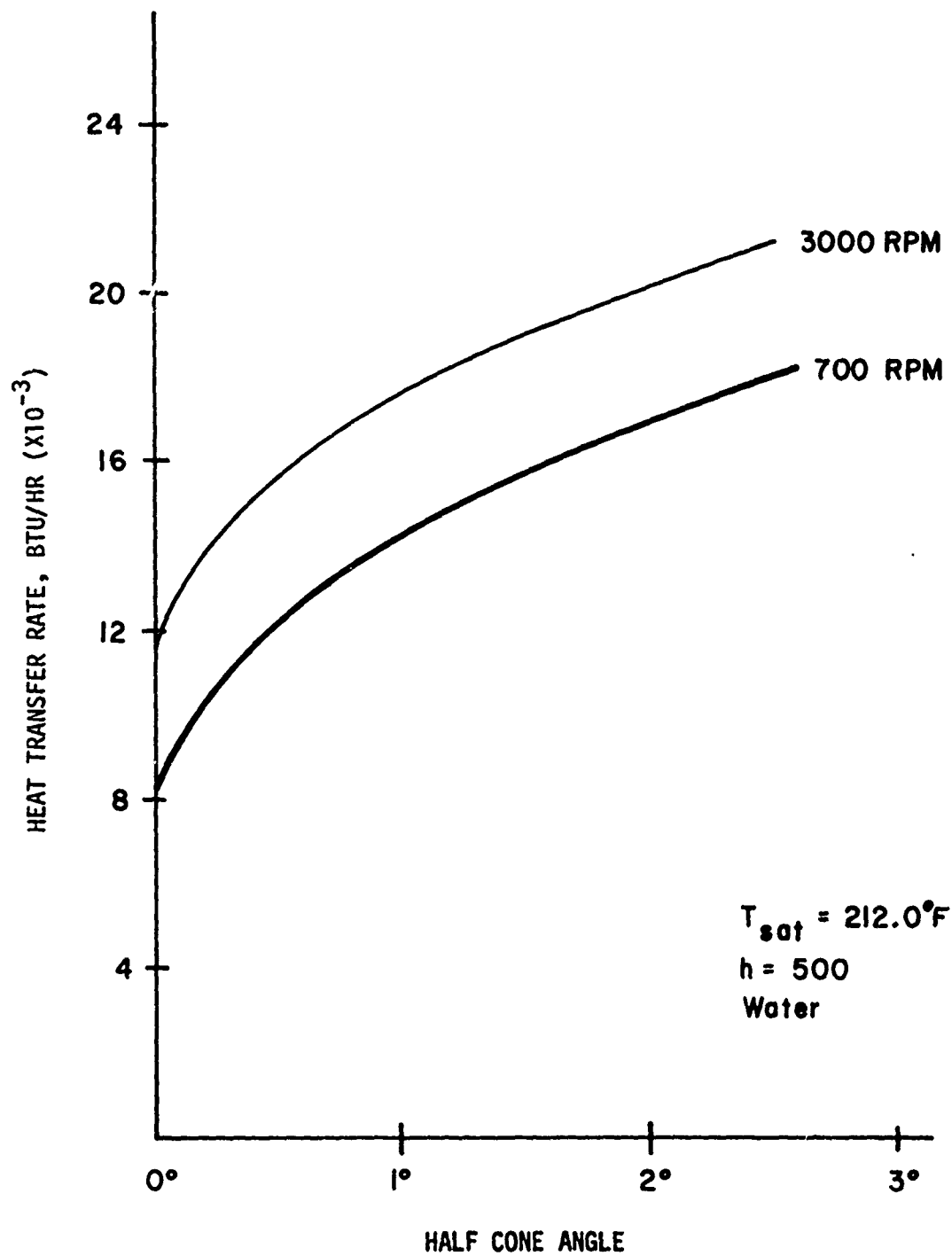


FIGURE 9 THEORETICAL HEAT TRANSFER RATE VS. HALF CONE ANGLE FOR WATER AT TWO ROTATIONAL SPEEDS

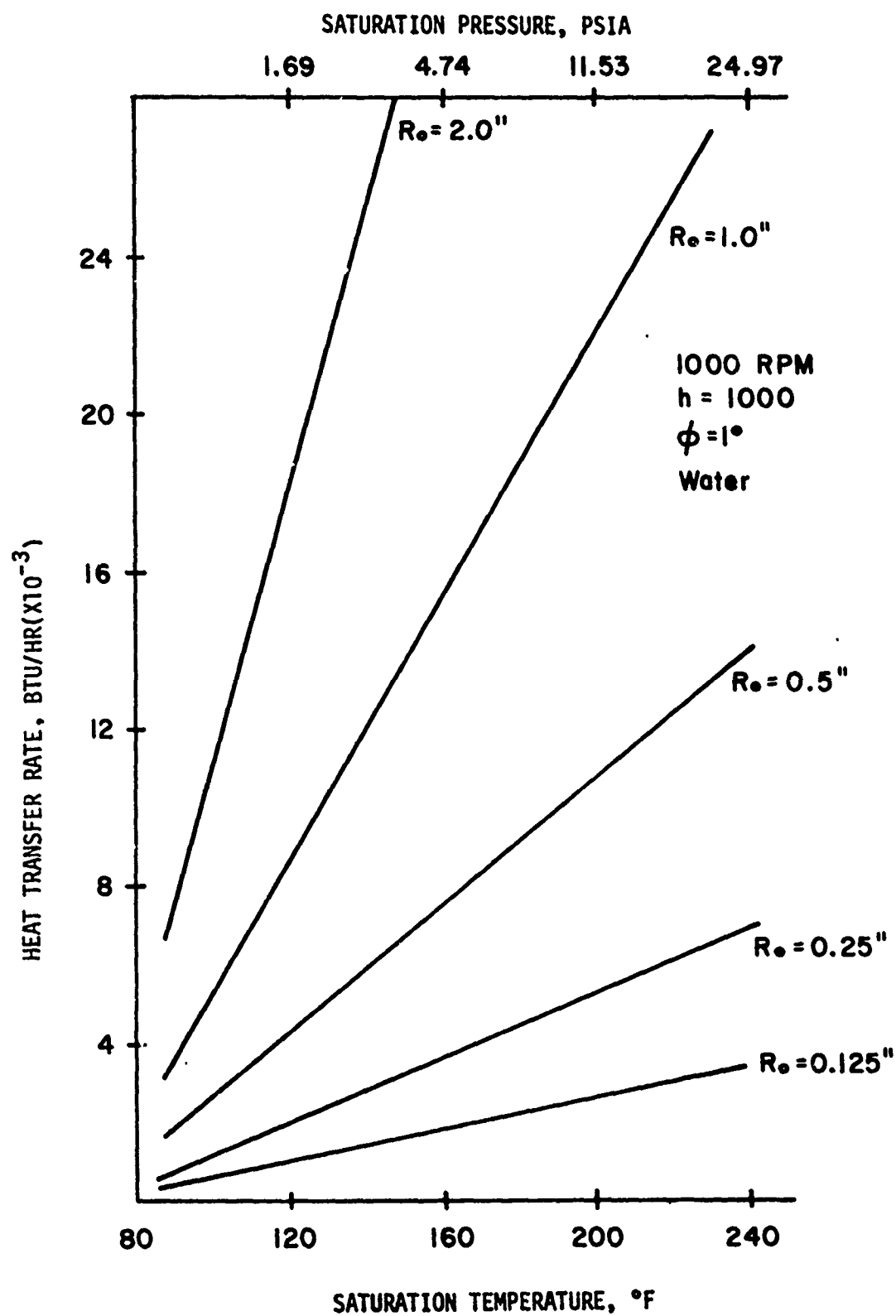


FIGURE 10 THEORETICAL HEAT TRANSFER RATE VS. SATURATION TEMPERATURE FOR
 WATER SHOWING INFLUENCE OF INTERNAL CONDENSER RADIUS

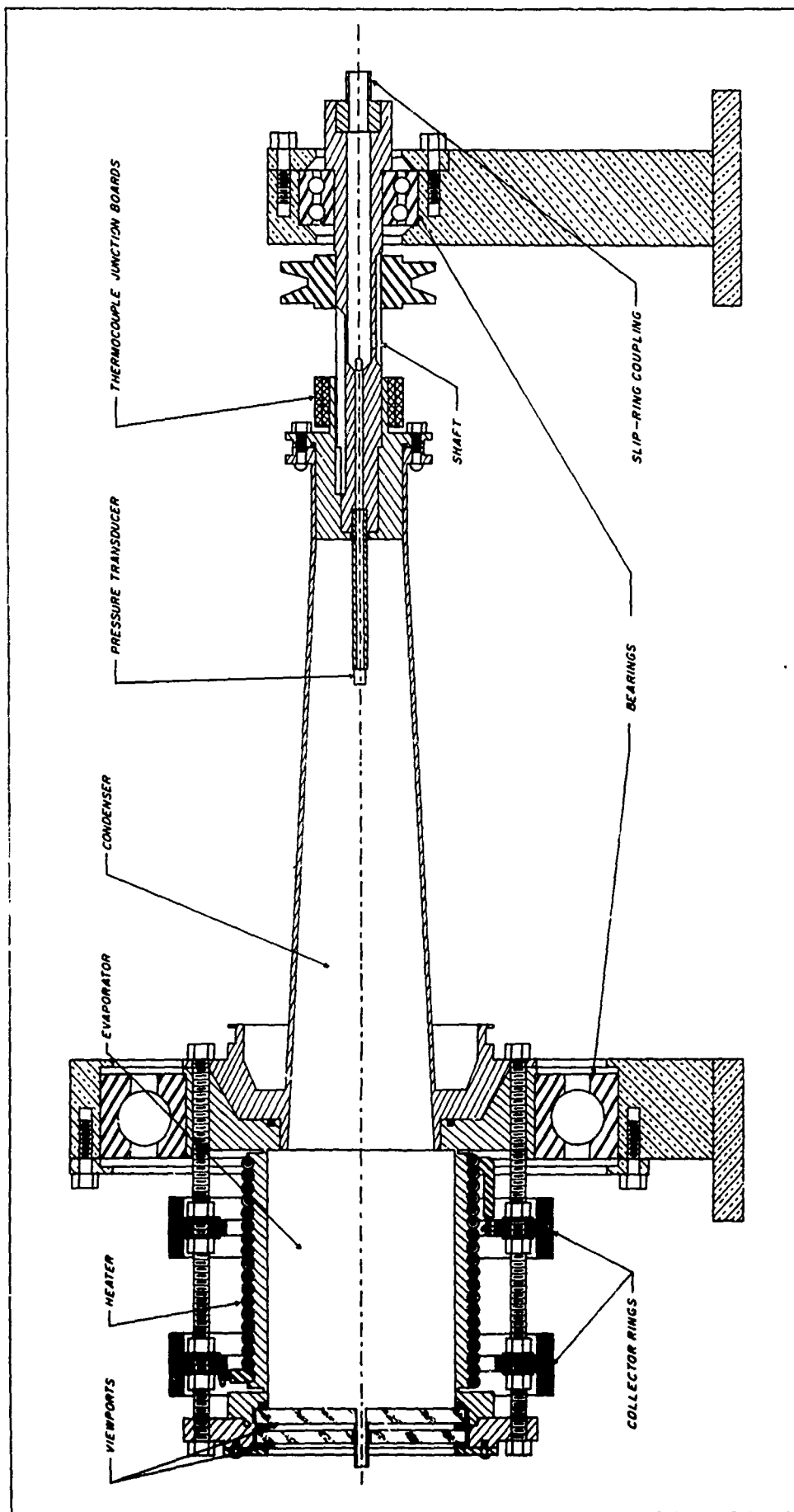


FIGURE 12. CROSS SECTION OF ROTATING HEAT PIPE

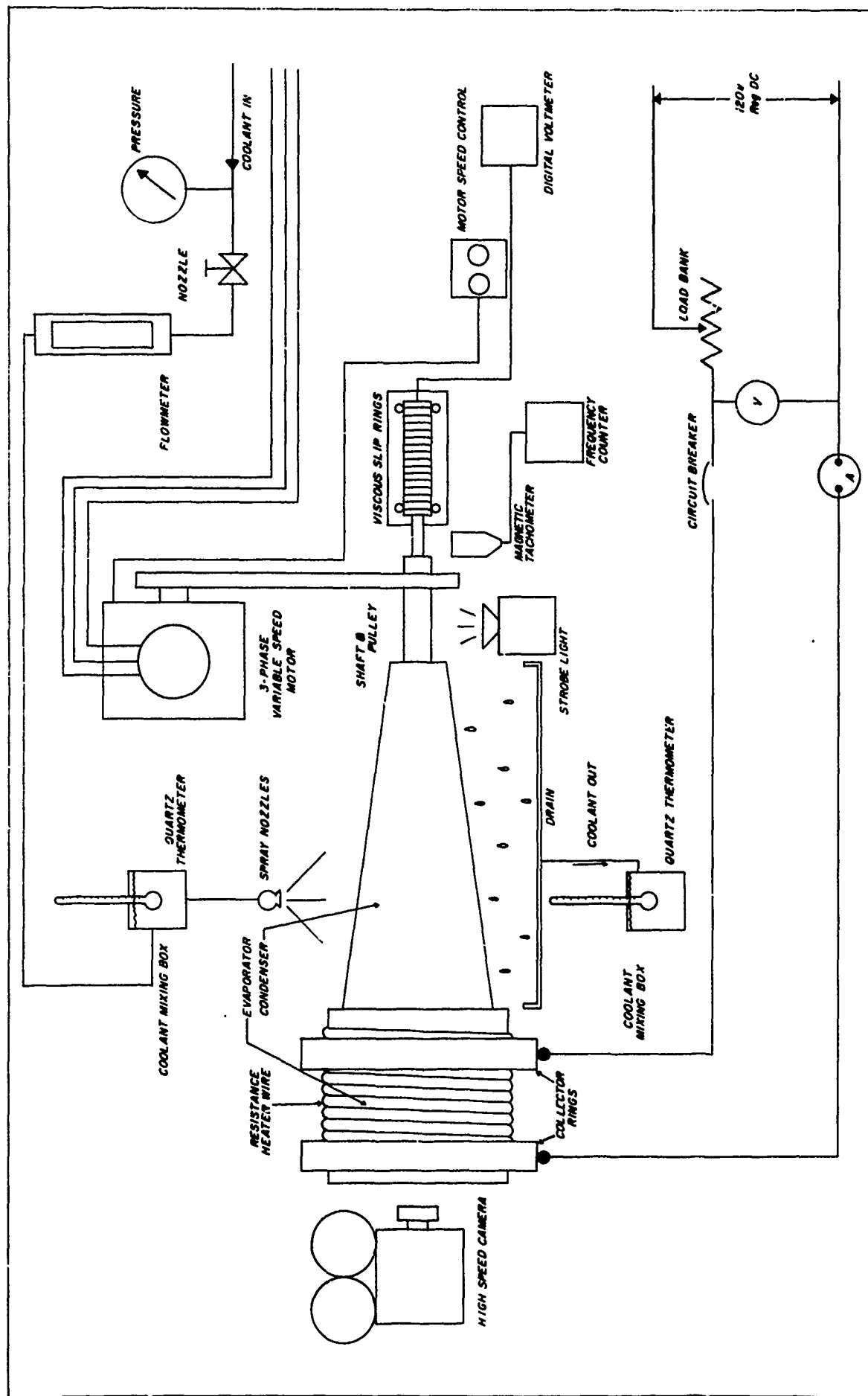


FIGURE 11. SCHEMATIC DIAGRAM OF EXPERIMENTAL EQUIPMENT.



FIGURE 13 PHOTOGRAPH OF THE EXPERIMENTAL FACILITY

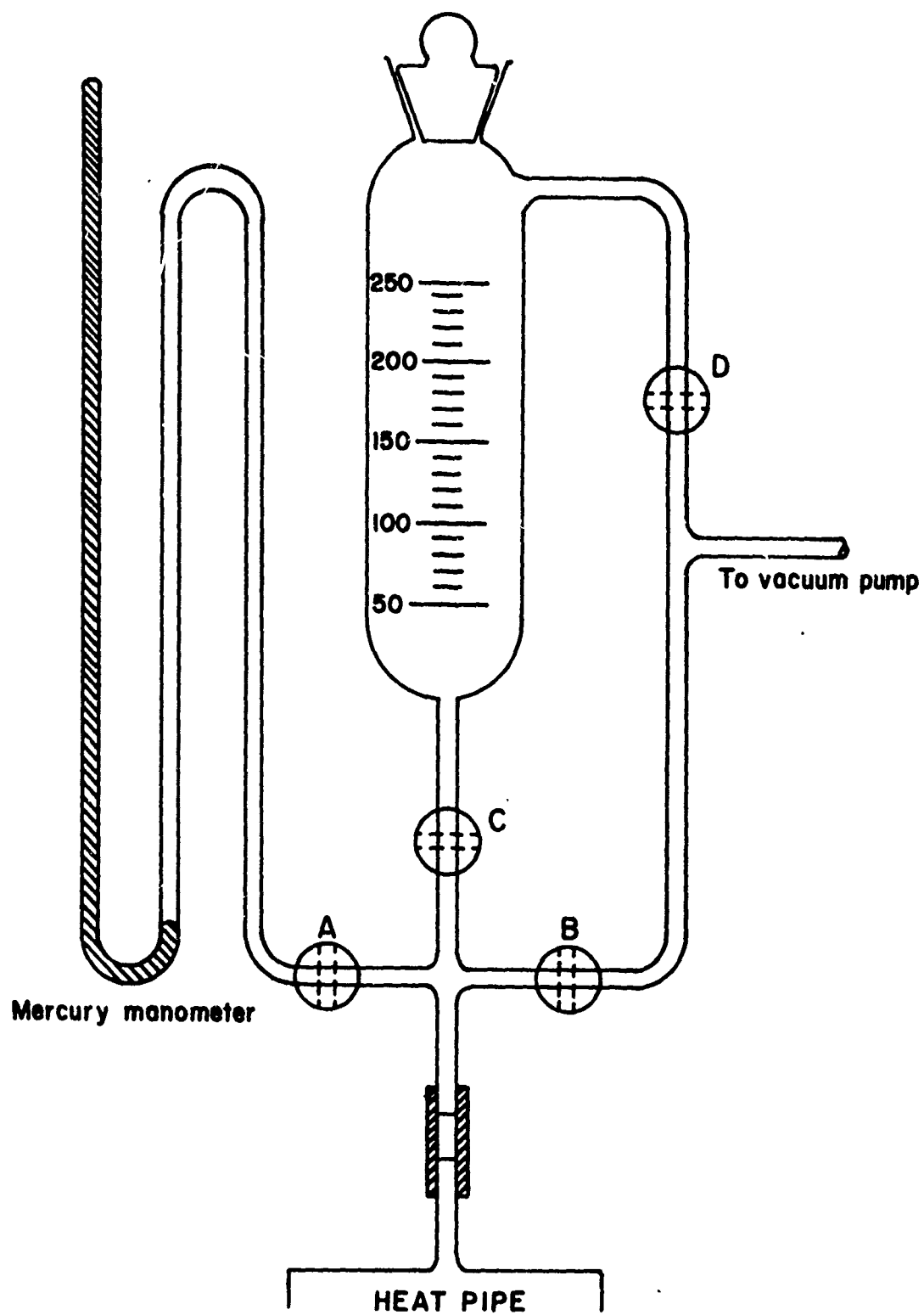


FIGURE 14 SCHEMATIC DIAGRAM OF FILLING SYSTEM

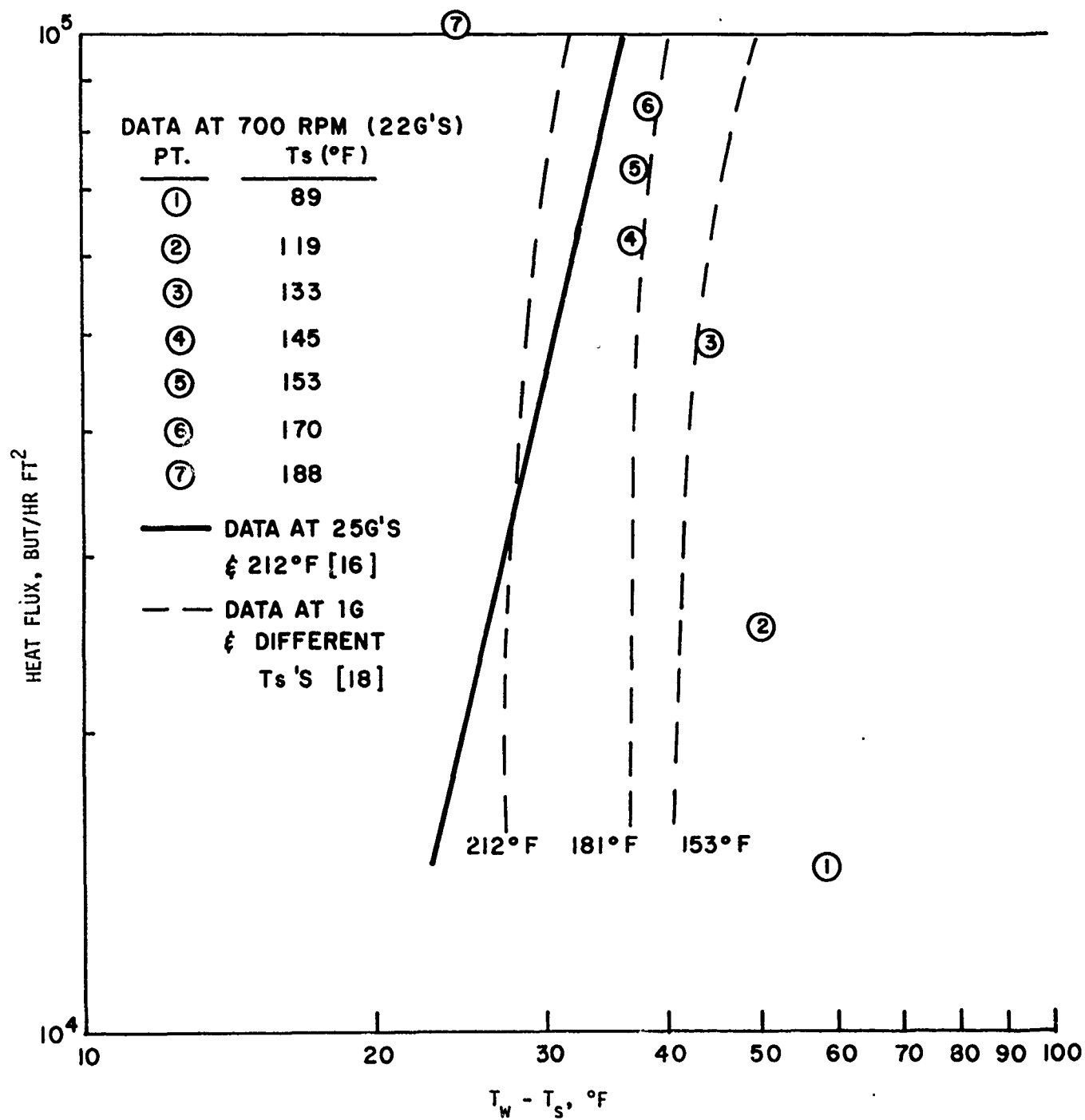


FIGURE 15 EVAPORATOR HEAT TRANSFER PERFORMANCE WITH DATA OF OTHER INVESTIGATIONS FOR COMPARISON

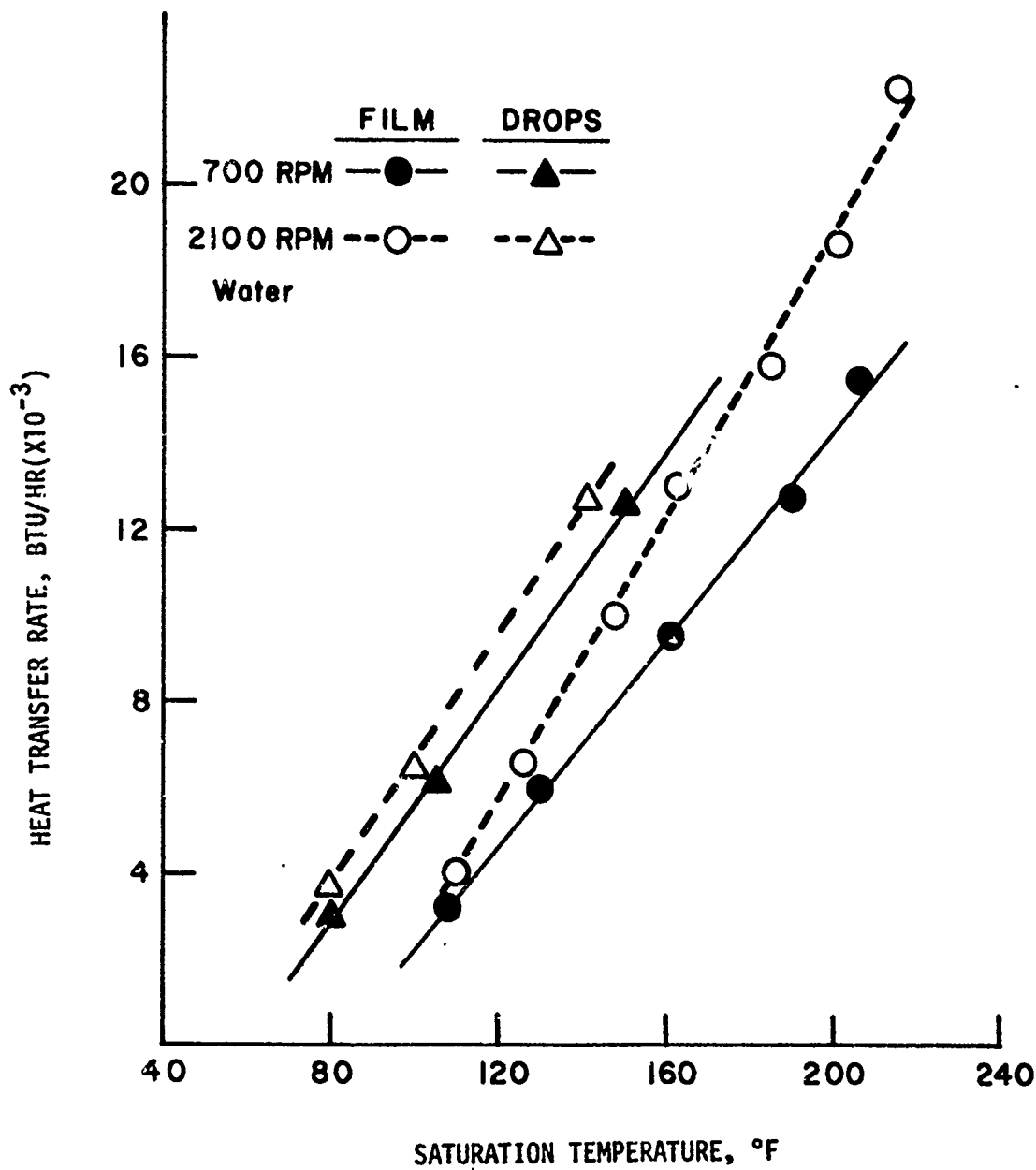


FIGURE 16 CONDENSER HEAT TRANSFER RATE VS. SATURATION TEMPERATURE
FOR FILM & DROPWISE CONDENSATION

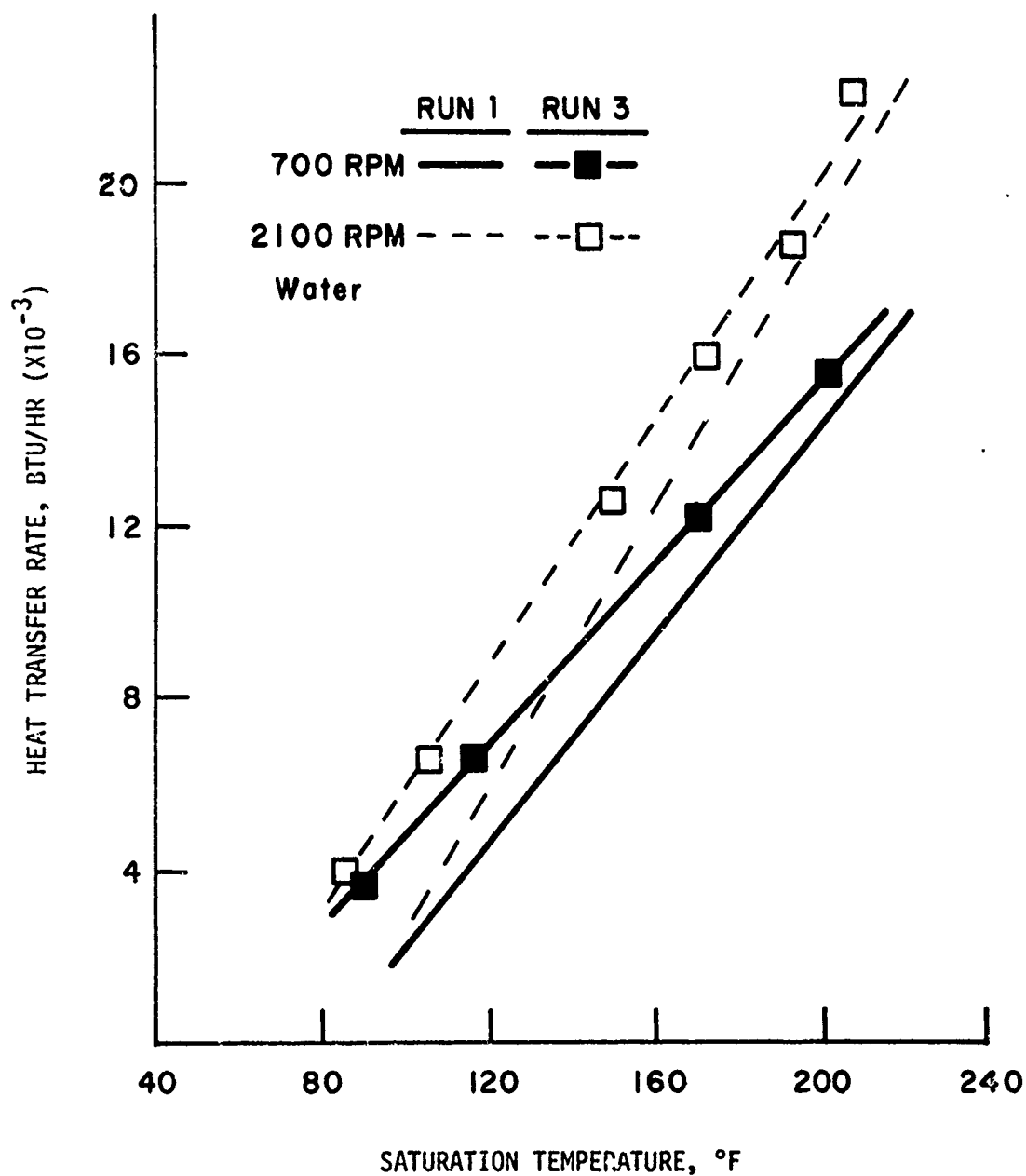


FIGURE 17 CONDENSER HEAT TRANSFER RATE VS. SATURATION TEMPERATURE SHOWING EFFECT OF FILLING PROCEDURE & PRESENCE OF NON-CONDENSIBLE GASES

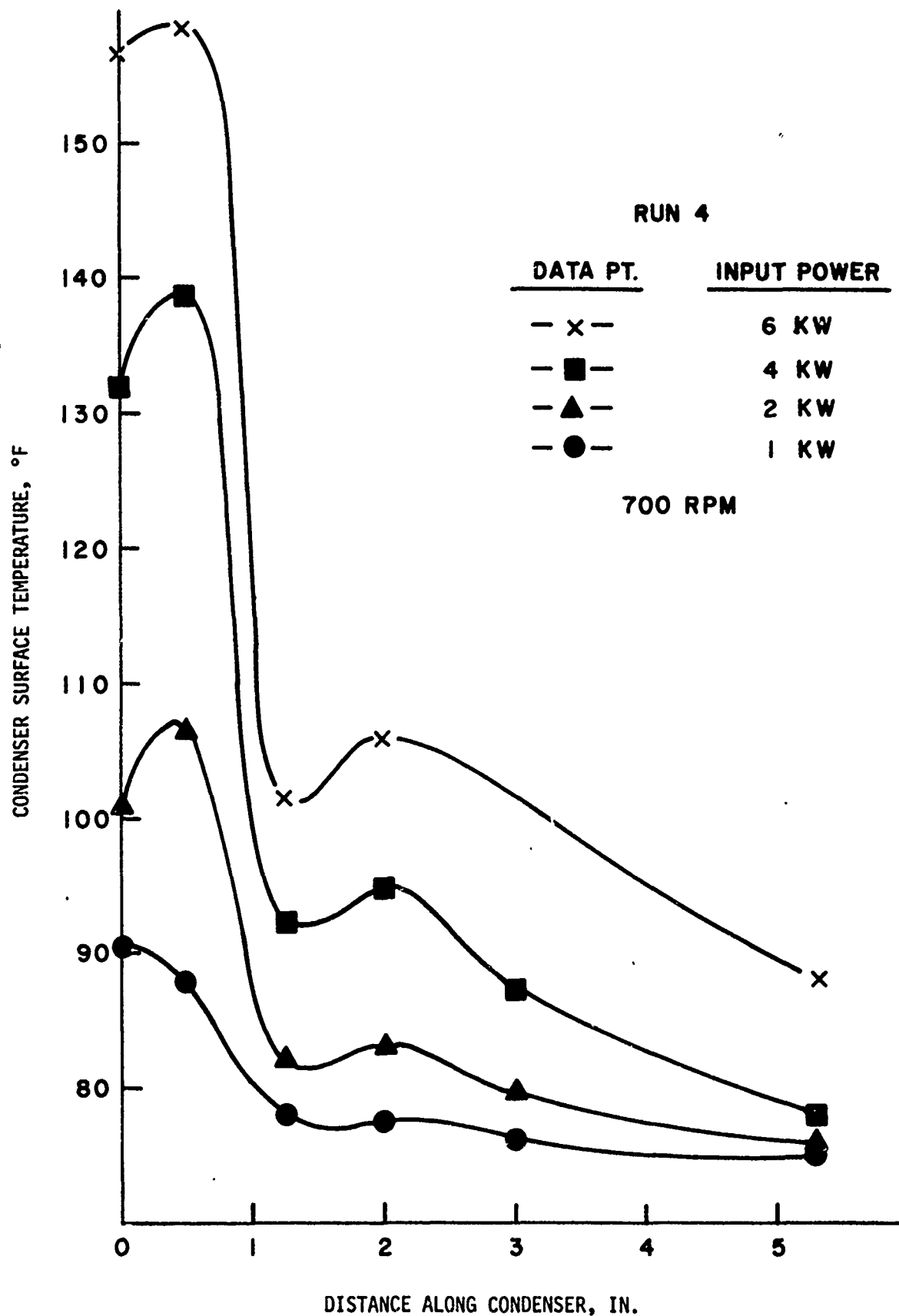


FIGURE 18 CONDENSER OUTSIDE SURFACE TEMPERATURE PROFILE AT 700 RPM

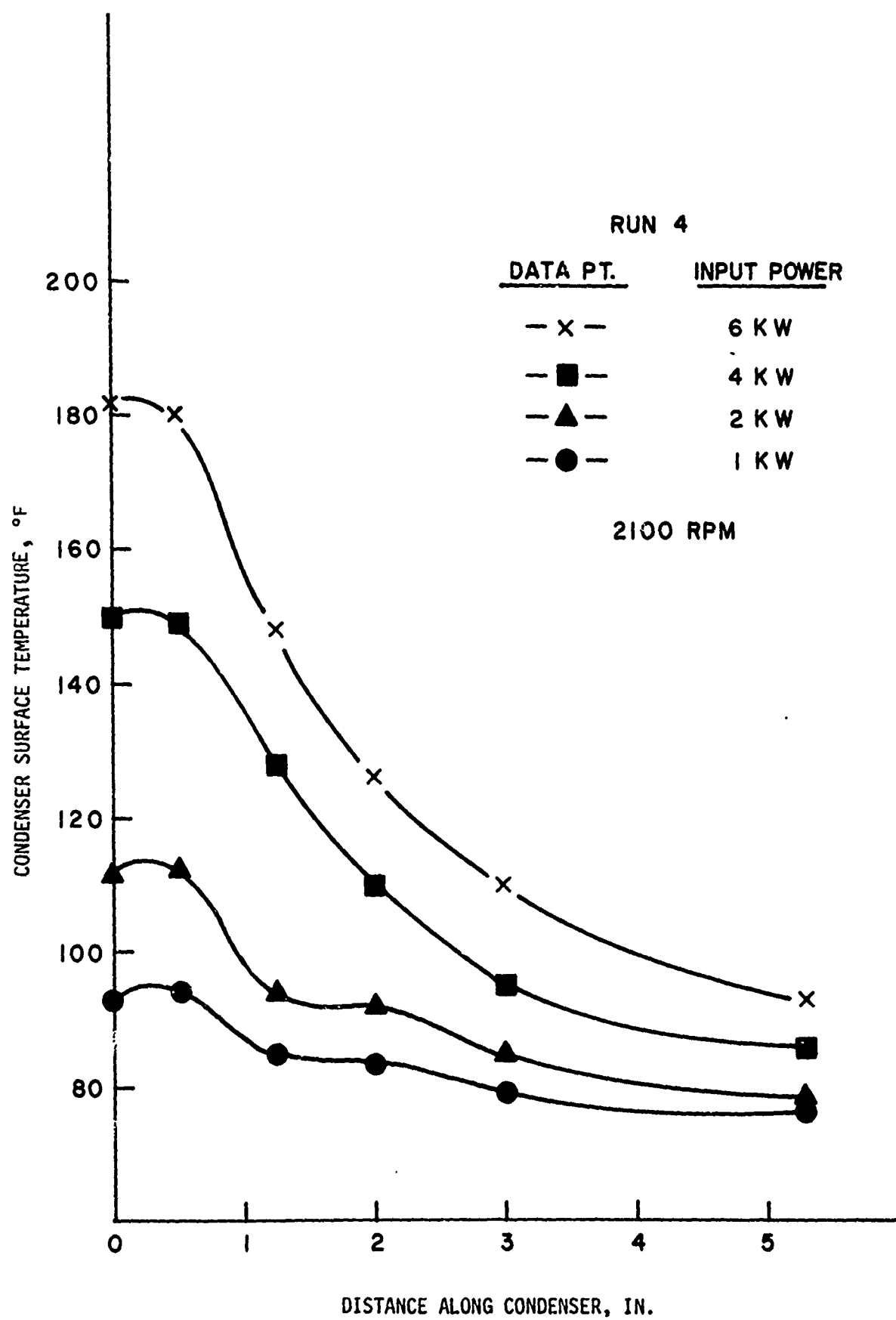


FIGURE 19 CONDENSER OUTSIDE SURFACE TEMPERATURE PROFILE AT 2100 RPM

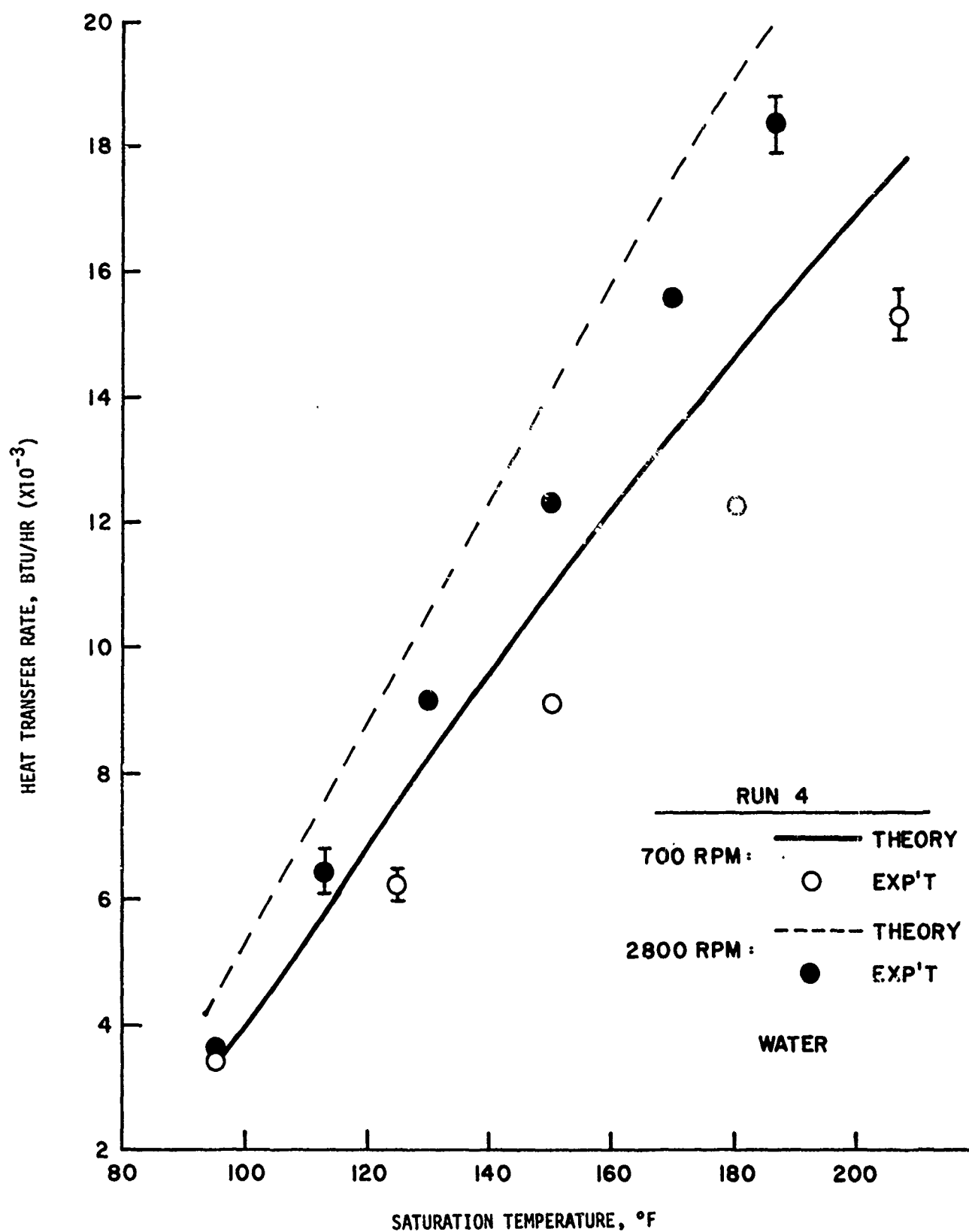


FIGURE 20 COMPARISON OF THE CONDENSER EXPERIMENTAL RESULTS WITH THE THEORETICAL PREDICTION FOR WATER

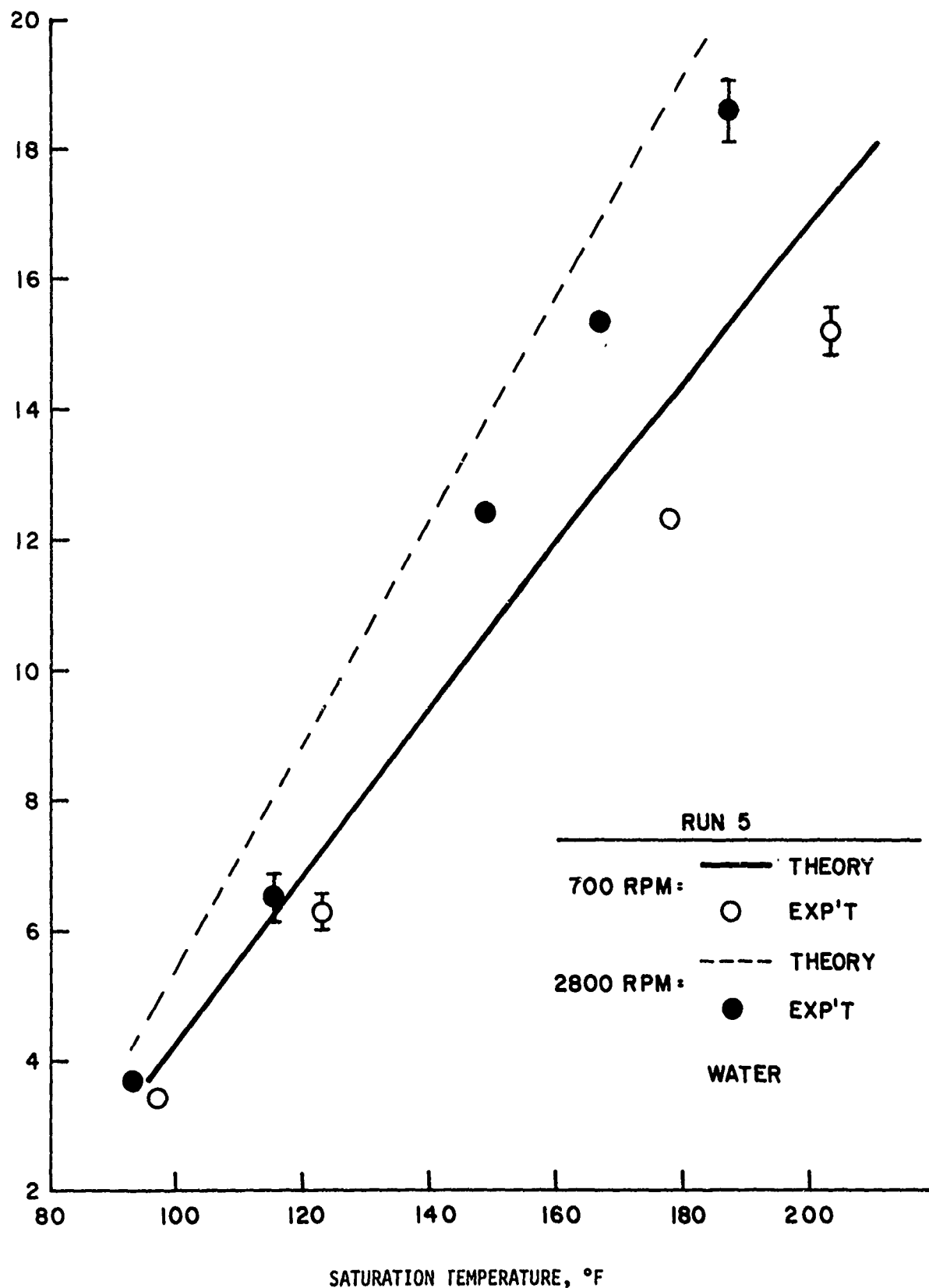


FIGURE 21 COMPARISON OF THE CONDENSER EXPERIMENTAL RESULTS WITH THE THEORETICAL PREDICTION FOR WATER

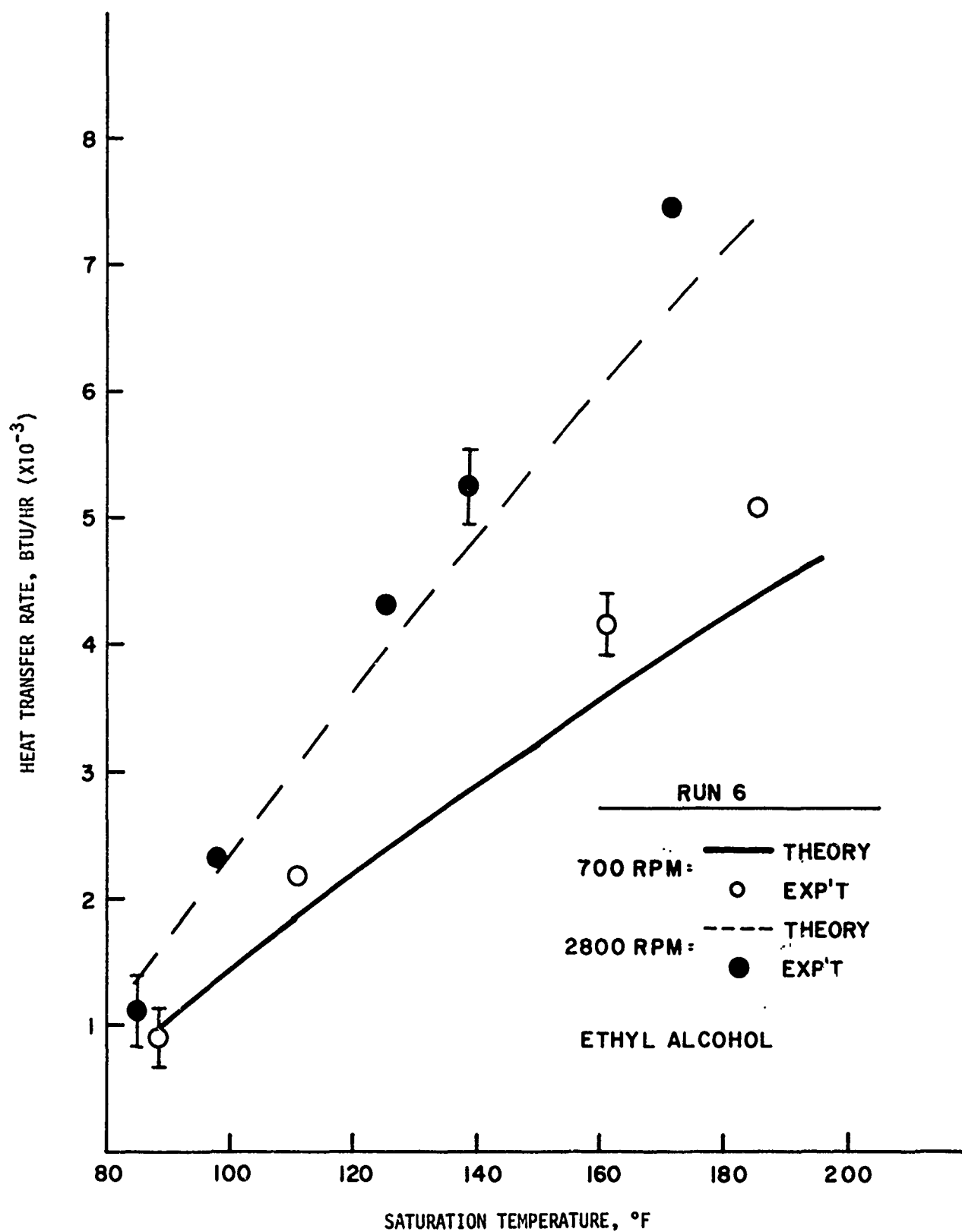


FIGURE 22 COMPARISON OF THE CONDENSER EXPERIMENTAL RESULTS WITH THE THEORETICAL PREDICTION FOR ETHYL ALCOHOL

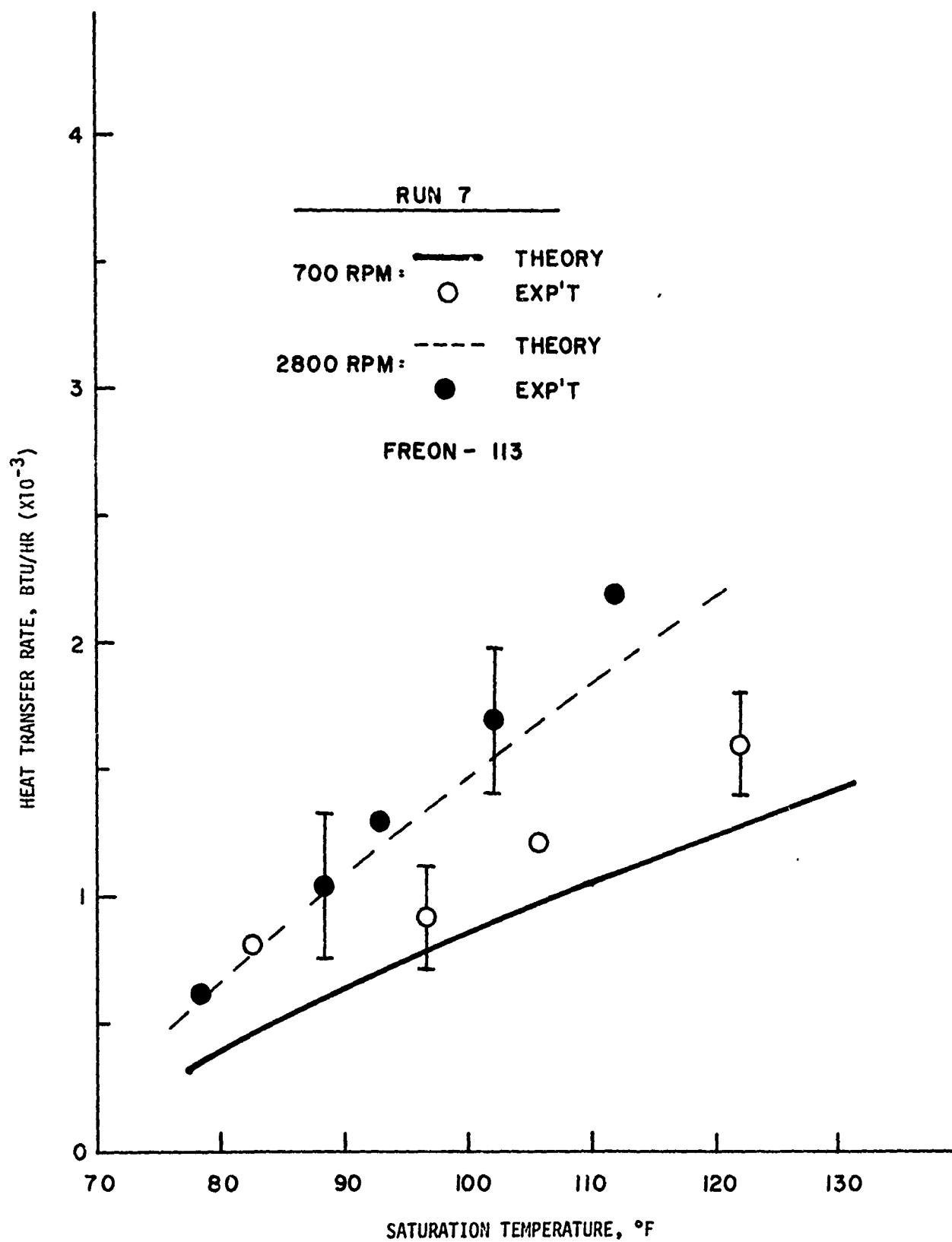


FIGURE 23 COMPARISON OF THE CONDENSER EXPERIMENTAL RESULTS WITH THE THEORETICAL PREDICTION FOR FREON - 113